TU Delft

Delft University of Technology

Document Version
Final published version

Licence
CC BY

Citation (APA)
Wang, Q., Feng, P., Wu, B., Teng, M., Jansen, K., & Bao, C. (2026). Multilayer jamming-reinforced inflatable systems for rapidly deployable lightweight construction. *Materials and Design*, *268*, Article 116573. https://doi.org/10.1016/j.matdes.2026.116573

Important note
To cite this publication, please use the final published version (if applicable).
Please check the document version above.

Copyright
In case the licence states “Dutch Copyright Act (Article 25fa)”, this publication was made available Green Open Access via the TU Delft Institutional Repository pursuant to Dutch Copyright Act (Article 25fa, the Taverne amendment). This provision does not affect copyright ownership.
Unless copyright is transferred by contract or statute, it remains with the copyright holder.

Sharing and reuse
Other than for strictly personal use, it is not permitted to download, forward or distribute the text or part of it, without the consent of the author(s) and/or copyright holder(s), unless the work is under an open content license such as Creative Commons.

Takedown policy
Please contact us and provide details if you believe this document breaches copyrights.
We will remove access to the work immediately and investigate your claim.

This work is downloaded from Delft University of Technology.

Materials & Design 268 (2026) 116573

Contents lists available at ScienceDirect

Materials & Design

journal homepage: www.elsevier.com/locate/matdes

Multilayer jamming-reinforced inflatable systems for rapidly deployable lightweight construction

Qinyu Wang [a], Peng Feng [a,*], Bo Wu [a], Mingrui Teng [a], Kaspar Jansen [b], Charun Bao [a]

[a] Key Laboratory of Civil Engineering Safety and Durability of Ministry of Education, Department of Civil Engineering, Tsinghua University, Beijing 100084, China
[b] Department of Sustainable Design Engineering, TU Delft, Delft 2628 CE, the Netherlands

ARTICLE INFO

Keywords:
Variable stiffness concept
Material stiffness
Multilayer jamming (MLJ)
Inflatable structures
Stiffness enhancement
Energy dissipation
Construction in extreme environments

ABSTRACT

Variable stiffness concepts enable structural adaptation through smart materials with inherent stiffness variation or innovative configuration-based designs using conventional materials. Among these, multilayer jamming (MLJ) provides rapid, reversible, and controllable stiffness modulation via vacuum-induced interlayer friction. This study proposes an MLJ-reinforced inflatable system for adaptive stiffening and enhanced energy dissipation in rapidly deployable lightweight structures. First, the influence of layer stiffness on MLJ performance is examined, identifying a suitable stiffness range for efficient reinforcement and providing guidance for material selection. A meter-scale prototype combining MLJ plates and an inflatable airbeam is then experimentally investigated under varying vacuum pressures, layer configurations, and loading conditions. The results show that vacuum activation significantly enhances stiffness and stabilizes the structure against collapse under reduced internal pressure. Quasi-static cyclic tests demonstrate that a 10 kPa vacuum condition achieves the best balance between stiffness enhancement, stable yielding, and energy dissipation, with dissipated energy increasing by 32–44% and ultimate load capacity by up to 38%. A simplified analytical model is developed to interpret stiffness evolution and the interaction between MLJ sliding and structural response. This work establishes MLJ as a scalable and designable material system for adaptive composite structures, with potential applications in construction, aerospace, and robotics.

1. Introduction

1.1. Variable-stiffness systems and multilayer jamming

Variable stiffness components have been applied in vibration control and large shape control. In vibration control, they can adjust structural dynamic characteristics to mitigate responses, while in large shape control, they enable structures to be flexible during programmed shape changes and rigid during load-bearing. Such components also allow structures to adapt to different states during transportation, construction, and service life [1,2]. Variable stiffness can generally be achieved through material-based approaches, such as shape memory polymers (SMPs) and magnetorheological elastomers (MREs), or configurational mechanisms, such as metamaterials, active bending, and jamming systems. SMPs undergo temperature-triggered glass transitions that enable significant reversible stiffness change (~96%) and damping enhancement (~11×) [3], and have been successfully implemented in rigidizable space gossamer structures [4–6]. In our previous work, SMP rigidization layers were investigated for lunar habitat concepts, where they helped prevent structural collapse and enhanced structural damping [7]. An analytical study on dual-layer beam systems further provided guidelines for optimizing the proportioning of variable- and constant-stiffness materials, ensuring the effective use of smart materials [8]. As a configurational variable stiffness mechanism, multilayer jamming (MLJ) increases out-of-plane bending stiffness through vacuum-induced interlayer friction. An MLJ system consists of multiple compliant layers (e.g., fabric, paper, or polymer sheets such as PET) stacked together and enclosed within an airtight envelope connected to a controllable pressure source [9,10], as shown in Fig. 1(a) [11]. The stiffness change of the MLJ system depends on interlayer slip states (pre-slip, partial-slip, full-slip) controlled by vacuum pressure and applied loads, as shown in Fig. 1 (b) [12]. This method offers significant advantages, including lightweight design, simple pneumatic control, rapid actuation, reversibility, structural recovery, adjustable stiffness, ease of shaping, and friction-based energy dissipation.

Existing MLJ systems have been predominantly applied in soft

* Corresponding author.
E-mail address: fengpeng@tsinghua.edu.cn (P. Feng).

https://doi.org/10.1016/j.matdes.2026.116573
Received 29 April 2026; Received in revised form 26 June 2026; Accepted 7 July 2026
Available online 8 July 2026
0264-1275/© 2026 The Authors. Published by Elsevier Ltd. This is an open access article under the CC BY license (http://creativecommons.org/licenses/by/4.0/).

robotics [14,15], human–machine interfaces, wearable devices [10,16–18], and medical instruments [11,19]. Most investigations focus on local stiffness variation, tip deflection control, or shape locking, rather than global structural performance such as load-bearing capacity, stability, or buckling behaviour. Moreover, their operation often requires relatively precise pneumatic regulation to maintain stable stiffness states and controllable transitions [14]. However, these applications are typically limited to millimetre–centimetre scales, and the application of MLJ in civil engineering or architectural structures remains largely unexplored. Existing studies rarely address system-level integration with load-bearing inflatable members, nor do they provide quantitative evaluation of global structural behaviour or design-oriented modelling frameworks. In particular, the influence of layer material stiffness on MLJ reinforcement efficiency has not been systematically investigated, and its role in structural-scale applications remains unclear. MLJ systems are typically constructed using flexible layers to enable interlayer sliding and deformation. However, the use of high-stiffness materials is also feasible. For example, Narang et al. [9] employed high-stiffness steel face layers combined with low-stiffness paper cores, achieving stiffness-to-mass ratios comparable to classical sandwich composites. By placing high-stiffness materials away from the neutral axis, a lever-arm effect can enhance stiffness variation. This raises a key question: what range of material stiffness is most suitable for MLJ systems? While flexible layers facilitate sliding, increasing stiffness may improve load-carrying capacity but reduce the effectiveness of the jamming mechanism. For sufficiently stiff materials, the reinforcement effect of MLJ may become limited, and the corresponding gain in load capacity requires clarification. Therefore, defining appropriate stiffness requirements for layered materials is essential for achieving high material efficiency in MLJ systems.

1.2. MLJ-reinforced inflatable structures and potential built-environment applications

Adaptive structures for extreme environments, such as polar regions or extraterrestrial surfaces, pose particularly stringent demands. For example, lunar structures must be lightweight for launch, compact for transport, and rapidly deployable under harsh, labour-limited conditions [20]. Inflatable habitats have thus emerged as a promising solution due to their advantages in transportation, storage, and rapid construction. However, their structural integrity relies on effective rigidization technologies to ensure mechanical stability after deployment and under potential air leakage [4,5,7]. The intrinsic characteristics of MLJ—including lightweight configuration, uniform pressure actuation, reversibility, and rapid response—suggest strong potential for integration with inflatable structural systems, where similar pneumatic principles are employed.

MLJ systems also offer potential for built-environment applications requiring rapid shaping, temporary fixation, and reversible stiffness control. For example, MLJ-based adaptive moulds could provide reusable and reconfigurable forming surfaces for curved composite components, reducing dependence on rigid single-geometry moulds. MLJ layers could also be incorporated into lightweight sandwich panels, allowing panels to remain flexible during transport and become rigid after installation. In addition, jamming-based media may serve as temporary self-forming templates for casting processes. These potential applications are illustrated schematically in Fig. 2.

For inflatable structures, MLJ layers can function as continuous reinforcement skins [21] or as localized stiffening ribs [22], depending on structural scale and loading requirements. Such configurations enable stiffness adaptation during transportation, deployment, and service. The integration of inflatable confinement pressure with layer-jamming reinforcement further suggests potential applications in extreme environments such as deep-sea or extraterrestrial habitats, where transportability, adaptability, and reusability are critical design considerations. MLJ can dissipate mechanical energy through interlayer friction during deformation. The force-displacement response of a simply supported MLJ beam component typically includes pre-slip, partial-slip, and full-slip stages [23], and the associated frictional sliding can produce pronounced hysteresis during cyclic loading. These characteristics indicate that MLJ systems may also function as adaptive energy-dissipating elements for vibration mitigation and impact-resistant structural systems.

1.3. Main contributions of this study

This research proposes an MLJ-reinforced inflatable system for rapid and automated construction in extreme environments or temporary missions. The main contributions of this study are as follows:

- A novel MLJ-reinforced inflatable structural system is proposed and demonstrated through a meter-scale prototype, extending multilayer jamming technology from millimetre–centimetre-scale components to structurally integrated systems relevant to civil engineering applications.
- The influence of layer stiffness on MLJ reinforcement efficiency is systematically investigated, and a suitable stiffness range is identified, guiding material selection and efficient utilisation of the MLJ mechanism.
- The stiffening capability of vacuum-activated MLJ reinforcement in inflatable structures is experimentally quantified. The effects of layer number, vacuum pressure, and loading conditions on stiffness and strength enhancement are systematically evaluated.
- The energy dissipation performance of the MLJ-reinforced inflatable system is investigated through quasi-static cyclic tests,

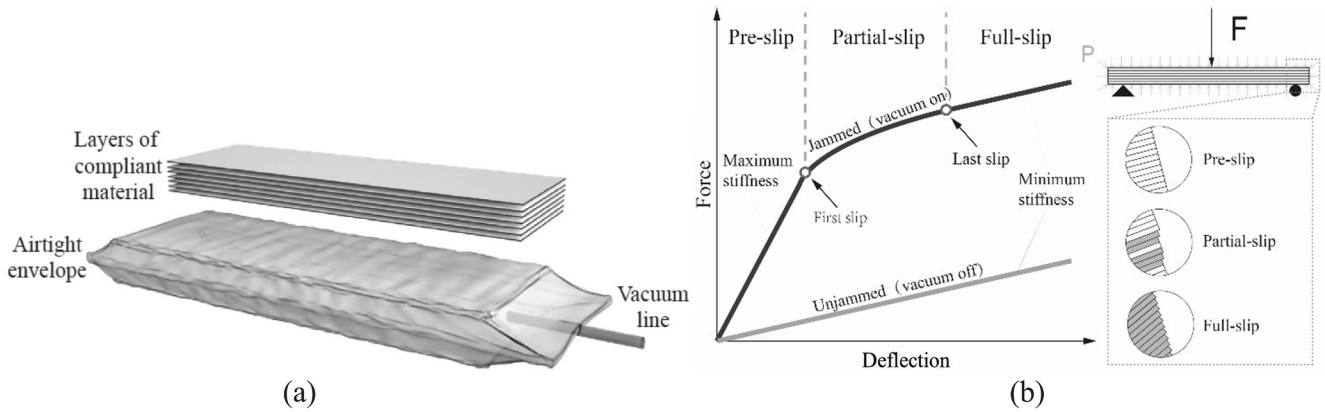


Fig. 1. (a) Composition of a multilayer jamming system [11]; (b) principle of a multilayer jamming (MLJ) system [12,13].

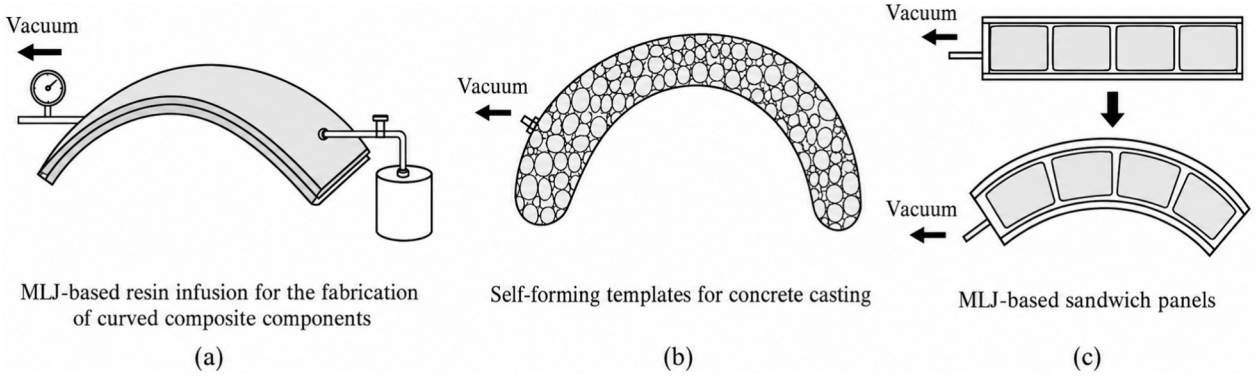


Fig. 2. Fast and self-forming: (a) MLJ-based resin infusion for the fabrication of curved composite components; (b) self-forming templates for concrete casting; and (c) MLJ-based sandwich panels.

demonstrating significant enhancement in hysteretic energy dissipation compared with conventional inflatable structures.

- The analysis of experiments provides mechanical insight and preliminary guidance for structural analysis and design calibration. The proposed system demonstrates potential applicability in deployable and inflatable structures across aerospace, construction, mechanical systems, and robotics, particularly for extreme or remote environments.

2. MLJ-compatible material window

This section provides a theoretical analysis of the influence of material stiffness on MLJ structural performance, and establishes fundamental principles for material selection in MLJ systems.

2.1. MLJ theoretical model

2.1.1. Linear stage: deflection–load relationship and interlayer shear

In the linear stage, no interlayer sliding occurs and the multilayer stack behaves approximately as a monolithic beam. The mid-span deflection is therefore governed by the number of layers n, the vacuum pressure (which determines the normal contact force between layers), and the intrinsic material stiffness (with or without considering the TPU outer layers). The analytical expressions in this section are applied only to the initial vacuum-on pre-slip stage of the MLJ plate and are used for parameter estimation, rather than for modelling the post-slip large-deformation behaviour.

For a simply supported n-layer beam, the load–deflection relationship is:

$$\omega_0 = \frac{FL^3}{48EI}, \tag{1}$$

where F is the applied load, L is the span, E is the Young's modulus of the sheet material, and I is the second moment of area:

$$I = \frac{b(nh)^3}{12}\left(= \frac{n^3}{12}bh^3\right) \tag{2}$$

As the load increases, the shear force within the stack increases. The maximum shear stress of the entire laminate is:

$$\tau_{max} = \frac{3F}{4nbh} \tag{3}$$

However, the maximum shear does not necessarily occur at the top or bottom interface. The interlayer shear stress at the ith interface (between layer i and $i+1$, counted from top to bottom) is

$$\tau_{inter,i} = \frac{3F}{4nbh}\left[1 - \left(\frac{2i}{n} - 1\right)^2\right] \tag{4}$$

Thus, the maximum interface shear occurs at $i = n/2$ for even n, or at $i = (n \pm 1)/2$ for odd n. The maximum interlayer shear is therefore

$$\tau_{inter,max} = \begin{cases} \dfrac{3F}{4bh}\dfrac{1}{n}, & n \text{ even} \\ \dfrac{3F}{4bh}\dfrac{n^2-1}{n^3}, & n \text{ odd} \end{cases} \tag{5}$$

For large values of n, the difference in maximum interlayer shear between the odd- and even-layer cases becomes negligible. However, for odd-layer stacks, the transition from the linear stage to the partial-sliding stage is considerably more complex. Sliding may initiate at either $i = n/2 + 1/2$ or $i = n/2 - 1/2$, and the sequence of sliding events becomes somewhat random. After each sliding initiation, the interlayer stresses redistribute before the next sliding event occurs, requiring multiple possible cases to be considered. This behaviour becomes complex and is not further examined in this study. For the even-layer case, however, the sliding process can be described more systematically. A detailed analysis for a four-layer stack is provided in the work of Caruso *et al.* [12], which serves as a useful reference for understanding the full evolution of the sliding process.

The maximum static friction force is governed by the interfacial friction coefficient μ and ΔP. Therefore, sliding initiates when

$$\tau_{inter,max} = \mu \Delta P \tag{6}$$

Combining Eqs. (1)–(5), the maximum deflection and load before the onset of sliding are given by

$$\omega_{max} = \frac{\mu \Delta P L^3}{3En^2h^2} \tag{7}$$

$$F_{max} = \frac{4}{3}nbh\mu\Delta P \tag{8}$$

For two fixed supports, the load–deflection relation becomes

$$\omega_0 = \frac{FL^3}{192EI} \tag{9}$$

Since the shear-force distribution remains identical to that of the simply supported case, the interlayer shear expressions remain unchanged.

$$\omega_{max} = \frac{\mu \Delta P L^3}{12En^2h^2} \tag{10}$$

$$F_{max} = \frac{4}{3}nbh\mu\Delta P \tag{11}$$

When the TPU outer membranes are considered, the modified load–deflection relationship and sliding limits are given in Appendix A.

2.1.2. Nonlinear stage: deflection–load relationship and interlayer shear after slip

After the first sliding event, the stiffness begins to decrease and the structural response becomes nonlinear. Caruso *et al.* [12] analysed the slip sequence of a four-layer stack and developed a general mechanical model describing sequential sliding in an n-layer system. Acevedo *et al.* [24] proposed a non-uniform delamination model based on Digital Image Correlation (DIC), which captures the elastic–plastic bending behaviour of jamming structures. By measuring the relative sliding displacement between each layer, the DIC-based method reconstructs the force–displacement response with higher accuracy; however, the measurements were taken at the free end of a cantilever beam, limiting the applicability of this approach to the present configuration.

In the composite structure examined here, the primary interest lies in predicting stiffness and yield capacity. Post-buckling behaviour and precise stiffness control are not required for the intended application, and therefore the detailed modelling of nonlinear sliding evolution is not further elaborated.

2.2. Material selection criteria based on stiffness

2.2.1. Material–structure regimes for MLJ systems

From Eqs. (7) and (8), it can be observed that the ultimate load capacity in the linear elastic regime is independent of material stiffness, whereas the material stiffness significantly influences the allowable deformation prior to the onset of interlayer slip. In particular, the maximum pre-slip deformation ω_{max} is inversely proportional to the material stiffness E. Consider a simply supported MLJ beam composed of identical laminae. Let ω_{μ} denote the ultimate deformation capacity of a single layer, and F_u the corresponding load capacity. Depending on the relative magnitude of the slip-initiation deformation ω_{max}, the allowable structural deformation ω_{allow}, and the material deformation capacity ω_u, six distinct behavioural regimes can be identified, as illustrated in Fig. 3. The regime map clarifies whether the MLJ mechanism mainly contributes to stiffness enhancement, frictional energy dissipation, or load-bearing improvement.

Effective MLJ performance requires interlayer slip to be activated within the allowable deformation range while maintaining sufficient reversibility and load-bearing capacity. Regimes (1) and (2) remain mainly in the pre-slip stage, where the jamming mechanism increases stiffness but does not activate frictional dissipation. Regimes (3) and (4) allow partial slip before the material deformation limit is reached; however, their effectiveness is limited by either high intrinsic stiffness or insufficient deformation capacity. Regime (5) represents high-stiffness materials with large reversible deformation, which may provide both stiffness and dissipation benefits but is uncommon in conventional monolithic materials. Regime (6), corresponding to low-stiffness and high-strain compliant materials, is therefore identified as the main design domain for MLJ systems, because it allows slip activation, reversible deformation, and meaningful load enhancement within the prescribed deformation limit. Table 1 summarizes the six regimes, representative materials, expected MLJ behaviour, and corresponding design implications.

It should be noted that the regime map in Fig. 3 is intended as qualitative material-selection guidance rather than a set of strict quantitative boundaries. The indicated stiffness ranges are approximate, and materials in intermediate ranges may also be used depending on specific design requirements. The areas shown in the figure do not represent the relative abundance of material types. In addition, all deformation considered here must remain within the elastic range; otherwise, irreversible deformation would reduce the recoverability and repeatability advantages of MLJ systems, and alternative structural strategies may be more appropriate.

2.2.2. Main design domain: Low-stiffness, high-strain compliant materials ($\omega_{max} < \omega_{allow} \ll \omega_u$)

This regime corresponds to the typical material selection in MLJ systems. For low-stiffness, high-strain compliant materials, failure is generally not governed by the intrinsic deformation limit of the material. Instead, the limit state is defined by the allowable structural deformation ω_{allow}, where $\omega_{allow} < \omega_u$.

After vacuum activation, the structure initially behaves in a fully coupled (jammed) state. As deformation increases to ω_{max}, the load reaches F_{max}, and interlayer slip is initiated. The sectional stiffness then decreases rapidly. Under continued loading, the structure deforms with the full-slip stiffness, which is approximately equal to that of the unjammed state, until the allowable deformation ω_{allow} is reached.

Since the slip behaviour in the partial-slip stage is difficult to predict, its contribution to strength enhancement is neglected in the present qualitative analysis. The ultimate load of the jammed structure is therefore approximated as the sum of the load at slip initiation and the additional load carried in the full-slip stage. Assuming linear elastic behaviour of each layer, the load–deformation relationship of a single layer can be expressed as

$$F_u(\omega) = k_u \omega \tag{12}$$

For a system composed of n identical layers:

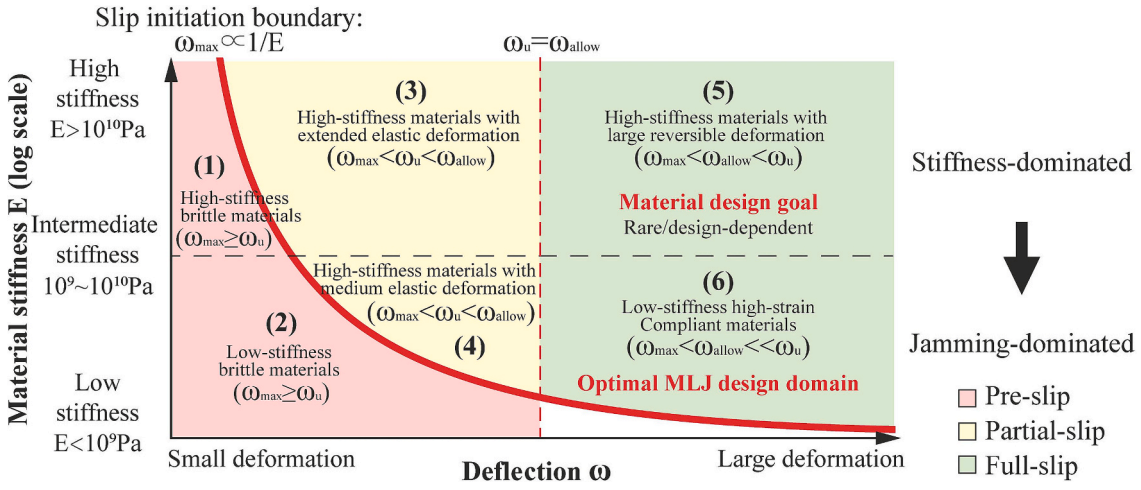


Fig. 3. Material–structure regime map for MLJ systems based on deformation compatibility, showing the applicable design domain for effective jamming behaviour.

Table 1
Summary of material–structure regimes for MLJ systems.

Regime	Material type	Possible materials	Expected MLJ behaviour	Design implication
(1)	High-stiffness brittle ($\omega_{max} \geq \omega_u$)	Metal sheets (e.g., steel, aluminium alloys) and high-modulus fibre-reinforced composites (e.g., CFRP laminates)	Pre-slip only; material failure before interlayer slip	Stiffness enhancement only; bonded sandwich structure may be more efficient if stiffness is the sole objective
(2)	Low-stiffness brittle ($\omega_{max} \geq \omega_u$)	Brittle polymer sheets (e.g., PMMA (acrylic), polystyrene (PS)), thin glass plates, and ceramic sheets	Failure before or near interlayer slip; limited load and deformation capacity	Generally unsuitable because jamming mechanism cannot be fully utilized
(3)	High-stiffness, extended elastic deformation ($\omega_{max} < \omega_u < \omega_{allow}$)	Thin metallic foils (e.g., stainless steel, aluminium, or copper foils) and tough composite laminates	Partial slip before material deformation limit; frictional dissipation possible	Mainly useful for energy dissipation; limited load enhancement
(4)	Low-stiffness, medium elastic deformation ($\omega_{max} < \omega_u < \omega_{allow}$)	Moderate-strain polymer sheets; coated fabrics with limited extensibility	Partial slip possible, but load capacity and dissipation are restricted	Limited practical effectiveness
(5)	High-stiffness, large reversible deformation ($\omega_{max} < \omega_{allow} < \omega_u$)	Architected materials, mechanical metamaterials, specially designed thin composite lattices	Slip activation with reversible deformation; stiffness modulation and energy dissipation	Promising but uncommon; requires special material or structural design.
(6)	Low-stiffness, high-strain compliant ($\omega_{max} < \omega_{allow} \ll \omega_u$)	Thermoplastic polyurethane sheets, silicone rubber sheets, elastomer-coated fabrics, flexible polymer films, nylon fabrics	Slip within allowable deformation; transition from jammed pre-slip to full-slip stage.	Main design domain; reversible stiffening, energy dissipation, and meaningful load enhancement.

Unjammed state:

$$F_{unjam}(\omega) = nk_u\omega \tag{13}$$

Jammed (pre-slip) state:

$$F_{jam}(\omega) = n^3k_u\omega, (\omega \ll \omega_{max}) \tag{14}$$

The load at slip initiation is

$$F_{max} = n^3k_u\omega_{max} \tag{15}$$

After slip, the structure behaves approximately as fully unjammed, and the ultimate load of the jammed system can be approximated as

$$F_{jam,ult} \approx F_{max} + nk_u(\omega_{allow} - \omega_{max}) \tag{16}$$

The corresponding ultimate load of the unjammed system is

$$F_{unjam,ult} = nk_u\omega_{allow} \tag{17}$$

The load enhancement ratio due to vacuum activation is therefore defined as

$$\Delta_F = \frac{F_{jam,ult}}{F_{unjam,ult}} - 1 \tag{18}$$

Substituting the above expressions yields

$$\Delta_F = \frac{n^3k_u\omega_{max} + nk_u(\omega_{allow} - \omega_{max})}{nk_u\omega_{allow}} - 1 = (n^2 - 1)\frac{\omega_{max}}{\omega_{allow}} \tag{19}$$

This result shows that the load enhancement depends on both the number of layers n and the ratio $\frac{\omega_{max}}{\omega_{allow}}$. Since $\omega_{max} \propto \frac{1}{E}$ and ω_{allow} is typically specified as a design constraint and can be treated as a constant, Δ_F decreases with increasing material stiffness.

For a given MLJ configuration, where the number of layers n, interfacial friction coefficient, and layer thickness are fixed, the slip initiation load F_{max} becomes a constant. When $\omega_{max} = \omega_{allow}$, the maximum load enhancement reaches its upper bound, i.e., $\Delta_F = n^2 - 1$. As the material stiffness increases, ω_{max} decreases, and the load enhancement provided by vacuum activation gradually diminishes, approaching zero in the limit of very high stiffness. Therefore, in this regime, lower-stiffness materials can achieve greater load enhancement through the jamming mechanism. From a design perspective, a minimum required enhancement ratio (e.g., 20%) can be specified. If the load enhancement achieved by vacuum activation falls below this threshold, the use of an MLJ system may not be justified, as the added complexity does not lead to sufficient structural benefit. Fig. 4 highlights the fundamental distinction between stiffness and load enhancement in

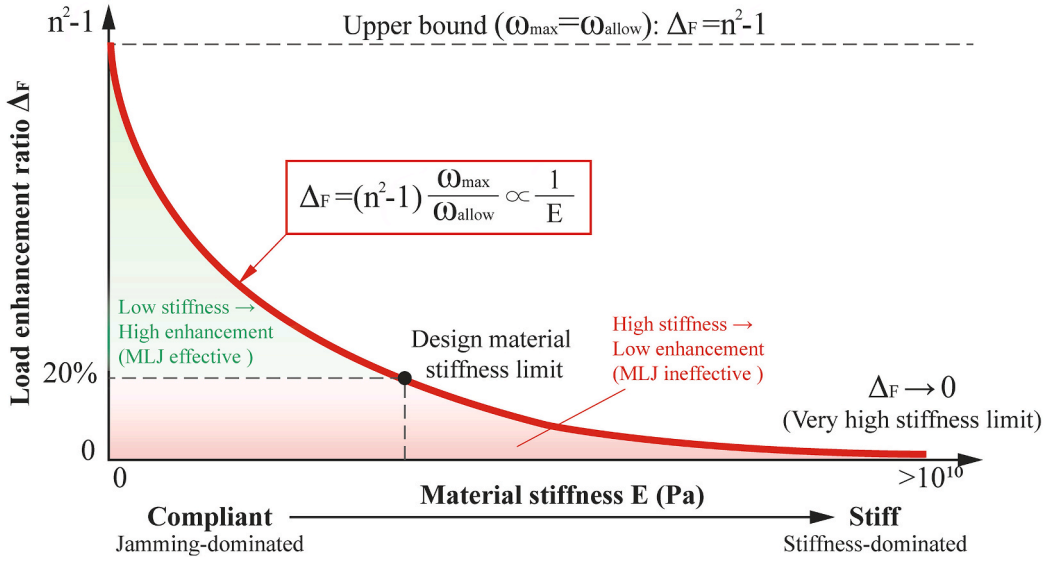


Fig. 4. Evolution of load enhancement ratio with structural deformation in MLJ systems.

MLJ systems: stiffness enhancement is governed by the interlayer coupling state, while load enhancement depends on both the slip initiation point and the allowable deformation.

2.3. Experimental stiffness control of MLJ plates: air pressure vs. stiffness

2.3.1. Experimental setup

Based on the material–structure regime analysis, the following experiments examine MLJ plates made of silicone-coated aramid fabric (SC-AF), a flexible and high-strain layered material suitable for reversible jamming behaviour. The plate-level tests are used to verify the expected deformation mode and transition from the jammed pre-slip stage to sliding-dominated behaviour, and to quantify the effects of vacuum pressure and layer number on stiffness and load capacity. These results provide component-level validation before the MLJ reinforcement is integrated with the inflatable structural system.

The experimental setup is shown in Fig. 5. The MLJ plates were tested in two configurations, with 10 and 20 layers of SC-AF fabric. Each plate measured 600 mm × 200 mm, and was laminated with a 1 mm-thick thermoplastic polyurethane (TPU) outer film with a hardness of 85 A (Fig. 5(d-f)). Stainless steel weights were used for loading, and midspan deflections were recorded under vacuum pressures of 0, −20, −40, −60, −80, and −100 kPa.

The specimen was mounted on two sliding rails, with one end fixed and the other horizontally movable, simulating simply supported conditions, as shown in Fig. 5(a). To minimize additional bending moments caused by lightweight clamps, an additional set of tests was performed with restrained end rotations. Accordingly, two boundary conditions were examined: (1) hinged supports at both ends, and (2) fixed-angle supports using bolted fixtures, as shown in Fig. 5(g-h). Vacuum pressure was controlled and measured by a digital pressure switch (*LFDS630; Lefoo Control Technology Co., Ltd., China*; −101∼0 kPa), connected to the vacuum pump and the integrated air nozzle (Fig. 5(b)). Vertical deflections were measured using a non-contact laser sensor (*HL-250-R; Jingjiake Intelligent Sensor Co., Ltd., China*; max. −165 mm) (Fig. 5(c)). Since the laser head was stationary, a flat reference plate was placed beneath the specimen to define the lowest point. Combined with the data of the laser sensor and the measured span length (via tape measure), this enabled calibration of the deflection data using large-deflection theory.

2.3.2. Results: mid-span displacement vs. air pressure & weight

This section reports deformation measurements of 10- and 20-layer MLJ plates under two support conditions (pinned and fixed-angle). The relationships among vacuum pressure, applied load, and midspan deflection were established. The corresponding displacement vs. weight curves are presented in Fig. 6, where both the midspan displacement and the support displacement are included to better represent the structural deformation behaviour.

For the first group (10-layer plate with hinged supports), when the load increased from 200 g to 500 g, the deflection suddenly exceeded the sensor range, and further measurements were not taken. Subsequent tests were therefore conducted using smaller weight increments. Across all tests—particularly under hinged conditions—abrupt large deflections were observed at certain load levels, surpassing the measurable range. Some intermediate measurement points were intentionally skipped when small, nearly linear deflections had already been confirmed at lower vacuum pressures, since further increases in vacuum were expected to produce only minor additional changes. Vacuum pressure was regulated using PID control. During testing, slight leakage caused the vacuum level to decay slowly, while the limited sensitivity of the pressure sensor and the high vacuum pump power introduced control challenges. A single evacuation could drive the pressure above −0.09 MPa almost instantly, requiring a waiting period until it returned to the target range. The control accuracy was within ±0.002 MPa; for example, at a nominal pressure of −0.02 MPa, the actual value fluctuated between −0.018 and −0.022 MPa. Matching a perfectly ideal vacuum was difficult, but the pressure could be stably maintained between −0.098 and −0.100 MPa.

Fig. 6 presents the force–displacement curves under different vacuum pressure levels, with each colour denoting a specific pressure. The applied loads were introduced as dead weights (in grams), while the plotted forces were obtained by converting the weights into equivalent forces using $F = mg$ with $g \approx 10\ m/s^2$. For the 10-layer plate with hinged supports, the structure exhibited almost no load-carrying capacity without vacuum, remaining soft and barely stable under self-weight and

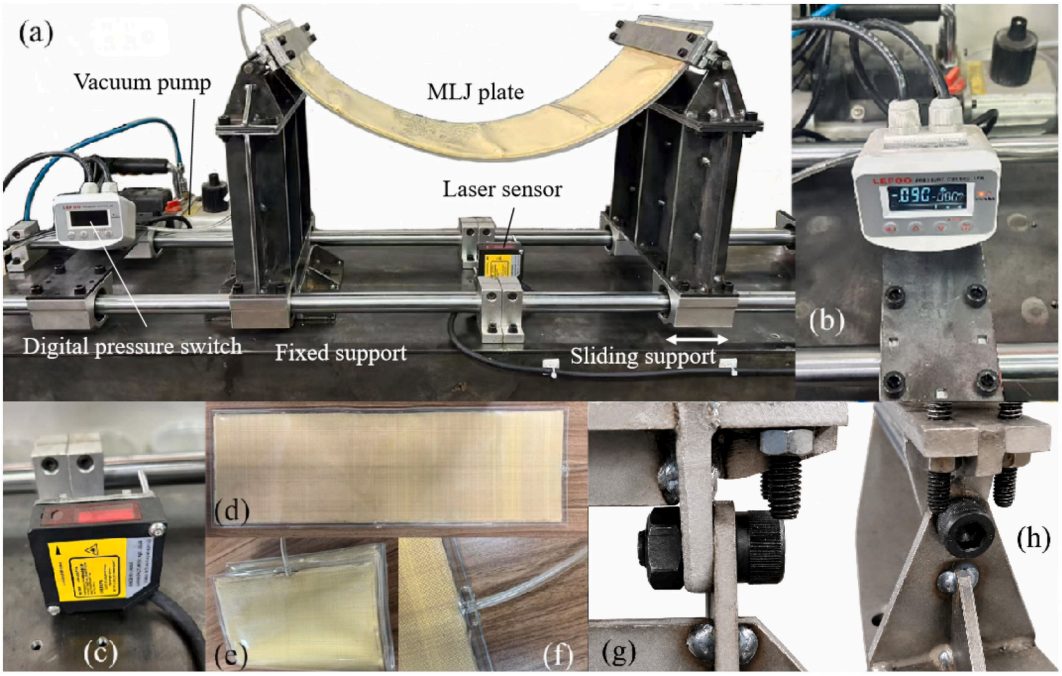


Fig. 5. Experimental setup: (a) testing system; (b) digital pressure switch (*LFDS630; Lefoo Control Technology Co., Ltd.; China*); (c) laser sensor (*HL-250-R; Jingjiake Intelligent Sensor Co., Ltd.; China*); (d-f) MLJ plate with integrated air nozzle; (g-h) fixed-angle support.

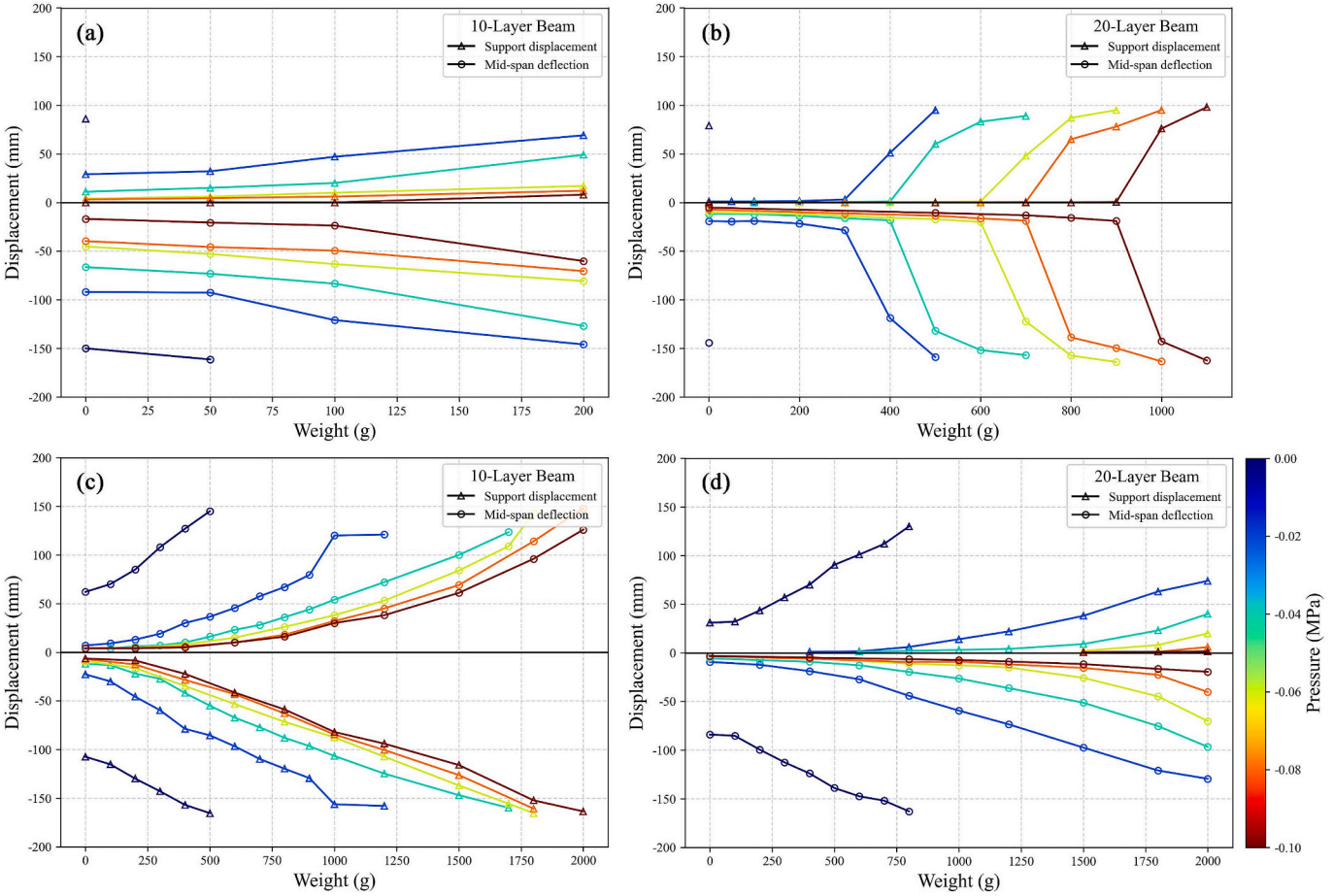


Fig. 6. Displacement vs. weight curves: (a) 10-layer hinged support; (b) 20-layer hinged support; (c) 10-layer fixed-angle support; (d) 20-layer fixed-angle support.

fixture-induced bending moments. Once vacuum was applied, even at as low as −0.02 MPa, stiffness increased markedly and the plate felt rigid to the touch. At 200 g (2 N), the response remained largely within the elastic range, as shown in Fig. 6(a). For the 20-layer plate with hinged supports, linear elastic behaviour was observed up to about 300 g under vacuum, with no interlayer slip. Across different pressure levels, higher vacuum extended the linear elastic region, while the overall curve shapes remained similar. In all cases, a sudden "kink" appeared, followed by rapid deflection growth and eventual stabilization beyond the sensor range, as illustrated in Fig. 6(b). To reduce the influence of fixture-induced end moments, additional tests were performed with fixed-angle supports. In this case, no distinct kinks were observed; instead, deflection increased gradually with load and vacuum level, showing an approximately linear response (Fig. 6(c) and (d)). Detailed interpretation of these behaviours is provided in the next section on failure modes.

Using the experimental data in Section 2.3.2, the effective interlayer friction coefficient μ was estimated using Eq. (A7), accounting for the TPU outer membranes:

$$\frac{4}{3}b\left(nh+2h_0\right)\mu\Delta P = mg \tag{20}$$

Because the loading process was applied stepwise rather than continuous, the exact load corresponding to instability onset cannot be identified accurately. Therefore, the calculated friction coefficient should be interpreted as an effective parameter rather than a uniquely defined material constant. Nevertheless, values derived from multiple tests provide reasonable ranges for interpreting structural behaviour and supporting model-based analysis. Similarly, the equivalent elastic modulus was evaluated using Eq. (1). Comparing the equivalent modulus with the tensile modulus of the aramid fabric enables assessment of material utilisation and consistency among experimental groups. The calculated parameters are reported in Table 2.

For the 20-layer hinged series, with interlayer pressure ΔP, the slope of the force–deflection curve k and the corresponding equivalent elastic modulus varied within the range of 0.36–0.49 GPa, while the back-calculated friction coefficient ranged from 0.045 to 0.077. For the 20-layer fixed series, the equivalent elastic modulus increased from approximately 0.05 GPa to 0.22 GPa with increasing ΔP, remaining significantly lower than the tensile modulus of the aramid fabric (0.13–0.58 GPa). These results indicate that the layer-jamming configuration cannot fully exploit the tensile capacity of the internal aramid fabric layers. In addition, the effective interlayer friction coefficient varies with confining pressure and boundary conditions. The material utilisation efficiency and the qualitative interpretation of these results are further discussed in Section 4.

2.3.3. Experimental observations of deformation behaviour of MLJ plates under increasing weights

The observed deformation behaviours of MLJ plates under increasing weight are summarized as follows:

- **Simply supported – low initial stiffness (10-layer, corresponding to steeper deflection–weight curves):** Plates with lower stiffness exhibited global deformation prior to any localized bending concentration. The test was terminated when excessive midspan deflection exceeded the measurement range, as shown in Fig. 7(a). In this state, even small additional loads caused disproportionately large displacements, indicating loss of load-carrying capacity. At

Table 2
Calculated parameters: equivalent modulus, SC-AF modulus, ultimate weight, and friction coefficient.

$\Delta P(MPa)$	20-layer hinged supports					20-layer fixed supports				
	0.02	0.04	0.06	0.08	0.10	0.02	0.04	0.06	0.08	0.10
Slope k (mm/g)	0.013	0.015	0.013	0.013	0.011	0.022	0.014	0.01	0.008	0.005
Equivalent modulus (GPa)	0.437	0.362	0.411	0.430	0.488	0.054	0.084	0.119	0.158	0.224
SC-AF modulus (GPa)	1.143	0.944	1.074	1.12	1.279	0.126	0.206	0.299	0.403	0.578
Ultimate weight (g)	300	400	600	700	900	–	–	–	–	–
Friction coefficient	0.077	0.051	0.051	0.045	0.046	–	–	–	–	–

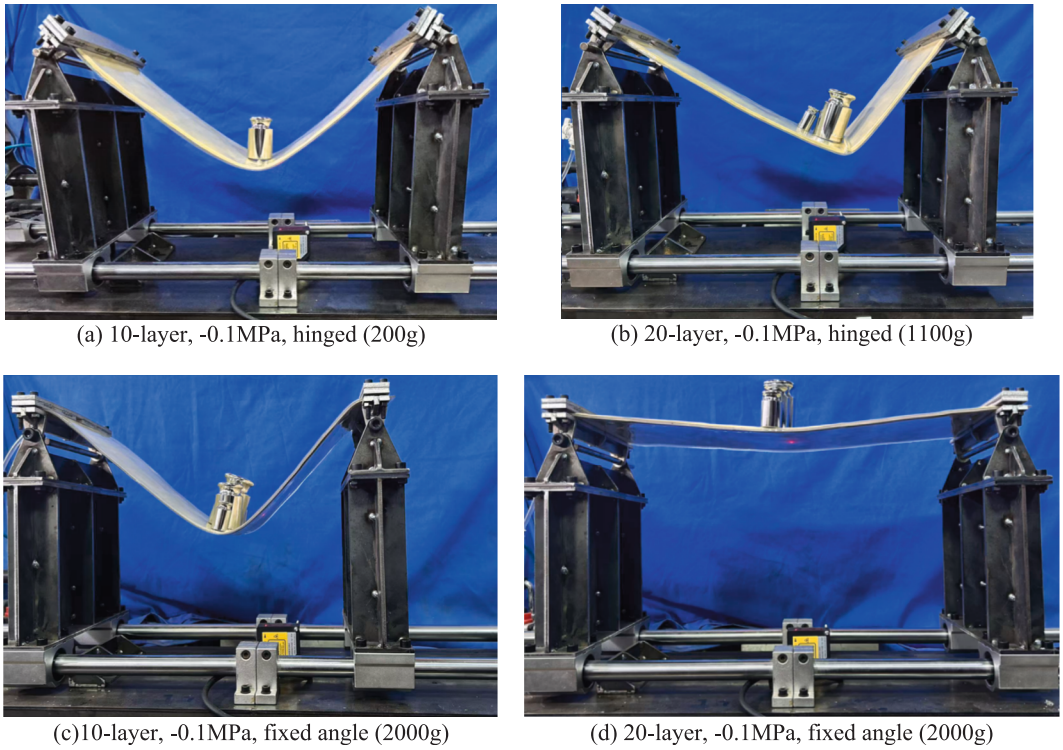

(a) 10-layer, -0.1MPa, hinged (200g)
(b) 20-layer, -0.1MPa, hinged (1100g)
(c)10-layer, -0.1MPa, fixed angle (2000g)
(d) 20-layer, -0.1MPa, fixed angle (2000g)

Fig. 7. Failure modes under full vacuum (−0.1 MPa) at extreme load levels within the measurement range: (a) 10-layer plate with hinged supports at 200 g; (b) 20-layer plate with hinged supports at 1100 g; (c) 10-layer plate with fixed-angle supports at 2000 g; (d) 20-layer plate with fixed-angle supports at 2000 g.

large deformation levels, the plate adopted a cable-like configuration resembling a catenary response. This behaviour results from the experimental boundary condition: the MLJ plate was clamped between rigid plates that were connected to supports capable of rotation and sliding, which were used to simulate simply supported boundary conditions.

- **Simply supported – high initial stiffness (20-layer, corresponding to flatter deflection–weight curves):** Plates with higher initial stiffness exhibited localized hinge-like deformation due to imperfections (e.g., internal layer wrinkles), as shown in Fig. 7(b). These localized bending zones caused sudden stiffness reduction and rapid increase in displacement. The distinct "kinks" observed in the weight–deflection curves (Fig. 6(b)) correspond to this instability transition rather than material plastic yielding. The behaviour is primarily associated with interlayer slip redistribution under vacuum confinement.
- **Fixed-angle supports (10- and 20-layer):** For specimens with restrained end rotations, no sudden local instability was detected (Fig. 7(c) and (d)). End restraint introduced additional bending resistance, enabling the plates to reach new equilibrium states after deformation. The interaction between horizontal forces generated by the restrained rotations and friction in the sliding rails allows the structure to stabilize at progressively larger deformation states. Even under the maximum applied load of 2000 g, the structural response remained stable without abrupt stiffness degradation, as reflected by the smooth displacement-weight curves in Fig. 6(c) and (d).
- **Creep-like effect under pressure control:** Under sustained loading combined with vacuum regulation, a creep-like deformation response was observed, particularly at higher load levels. Once deformed, constant vacuum pressure generated interlayer friction that effectively locked the structure in the deformed configuration. As a result, the stiffness during unloading corresponded to the vacuum-on pre-slide condition, and the structure could not fully recover its original flat shape. Subsequent loading applied on this already deformed configuration led to progressively larger displacements, indicating a geometric second-order effect. To ensure repeatability, each test group was reset to the flat state before reloading.
- **Recoverability:** All observed deformation states in the experiments were fully reversible. Upon vacuum release, the plates returned to a flexible state and recovered their original geometry after re-vacuuming, indicating that the observed behaviour corresponds to reversible instability rather than structural failure.

3. Multilayer jamming-reinforced inflatable systems

3.1. Concept and construction process

The proposed MLJ-reinforced inflatable beam consists of an airbeam, an upper MLJ plate, and spirally arranged aramid fibre ropes, as shown in Fig. 8(a). The airbeam provides the initial deployable form and pneumatic support, while the MLJ plate acts as a vacuum-activated stiffening layer. After vacuum activation, interlayer friction within the MLJ plate increases the bending stiffness of the upper reinforcement, thereby improving the load-bearing capacity and stability of the inflatable system. The aramid fibre ropes are introduced as lightweight tensile restraints to assist geometric stabilisation and force transfer, and can also serve as simple connection elements for assembling multiple units into larger deployable structural systems. Multiple units may therefore be connected in parallel to form lightweight roofs, temporary bridges, or floating platforms. [25]

The structure can be easily transported in a folded and rolled state and assembled through a simple pneumatic process. Fig. 8(b) illustrates the cyclic process of construction, service, and reuse with the following steps:

(1) **Unfolding:** Initially, the structure is unfolded and flattened.
(2) **Inflation:** The airbeam is inflated and pressurized, stretching the aramid fibre ropes to generate pre-tension. In this case, the structure is essentially formed and the top MLJ plate is fully expanded.
(3) **Vacuumizing:** After vacuuming, the top compression element of the structure is formed, enhancing the load-bearing capacity.
(4) **Service:** During service, multiple units can be connected in parallel using simple methods such as ropes and buckles. This versatile structure is suitable for extreme environments, shelters, or temporary event structures. To further increase the load-bearing capacity and extend the service life, resin can be introduced in the MLJ plate after vacuuming to form an FRP composite plate on the top. The air pressure in the airbeam can be regularly refilled, and the aramid fibre ropes, featuring easy connection mechanisms, can be swapped out when needed. This further enhances reparability.
(5) **Softening:** After service, the structure can be recycled for future use. The airbeam releases the gas, leading to its collapse. Subsequently, vacuum release softens the top of the MLJ plate. Alternatively, the vacuum can be released first from the MLJ plate, followed by deflating the airbeam.
(6) **Folding:** Now that the structure is in a soft state, it can be rolled up as a whole and stored in a backpack or other bags for convenient transport and future assembly.

3.2. Loading on an MLJ-reinforced inflatable beam

3.2.1. Experimental setup

The MLJ-reinforced inflatable beam prototype used in the experiments is shown in Fig. 9. To increase the effective contact area between the inflatable member and the MLJ reinforcement while maintaining fabrication feasibility, a rectangular airbeam configuration was adopted. The airbeam was fabricated from white nylon-reinforced TPU membrane using high-frequency welding to form a sealed inflatable chamber. The MLJ plate was manufactured with identical plan dimensions and attached to the upper surface of the airbeam along the two longitudinal edges through high-frequency welding. After inflation, internal pressure maintains the rectangular geometry of the airbeam while inducing a slightly curved upper surface. Consequently, the MLJ layer forms a shallow curved shell tightly coupled with the inflatable member, ensuring stable geometric conformity and efficient load transfer between the inflatable support and the jamming reinforcement.

The prototype had a total length of 1 m, with a width of 200 mm and an inflated height of approximately 100 mm. The inflatable envelope consisted of white nylon-reinforced TPU, providing improved tensile strength and pressure resistance, while the multilayer jamming component employed silicone-coated aramid fabric (SC-AF) layers with an individual layer thickness of approximately 0.26 mm [8]. The experimental system followed the same general configuration as the MLJ plate tests, including vacuum activation, pressure control, and midspan displacement measurement. A vacuum pump and digital pressure switch were used to control the vacuum pressure in the MLJ component, while an additional positive-pressure sensor was used to monitor the internal pressure of the lower airbeam. Midspan deflection was measured using the same non-contact laser displacement sensor, as shown in Fig. 9(a). The main modification was the support system: specially designed semi-cylindrical supports were adopted to accommodate the inflatable geometry and provide stable support to the airbeam, as illustrated in Fig. 9(b). Fig. 9(c) shows the undeformed and deformed anchorage holes in the TPU cover, illustrating the local deformation associated with the aramid fibre ropes during loading.

3.2.2. Load-bearing response and collapse resistance of MLJ-reinforced inflatable beams

To reduce stress concentration (as preliminary tests indicated that a smaller contact area led to a lower measured ultimate strength), a steel plate of 300 × 90 × 8 mm with an initial weight of 1693.6 g (17 N) was placed on the top surface as the loading interface, as shown in Fig. 10(d). Positioning bolts were introduced at the loading point to prevent eccentric loading and to avoid tilting of the steel plate, which could otherwise collide with the load cell and affect measurement accuracy. Four configurations were tested to evaluate the respective effects of

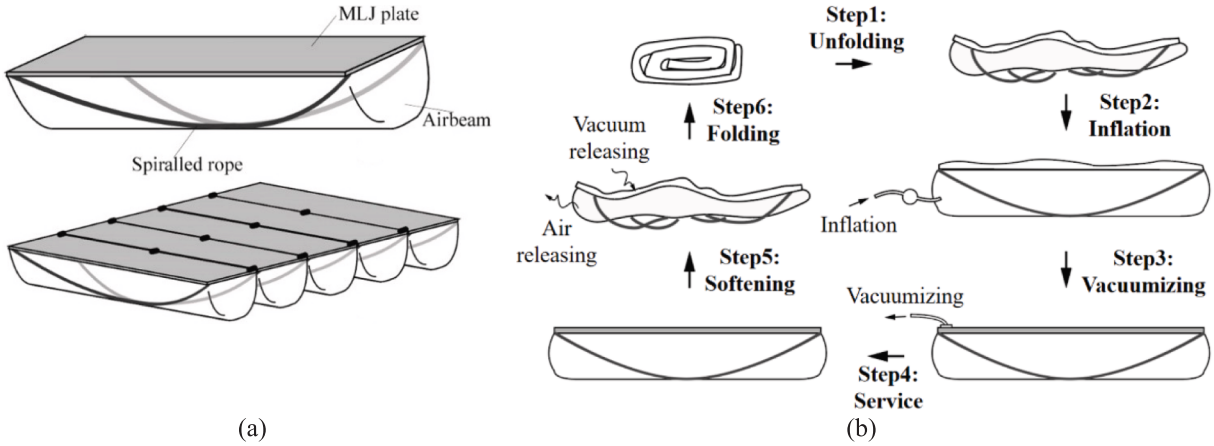


Fig. 8. MLJ-reinforced inflatable beam: (a) basic elements and combination; (b) construction process [25].

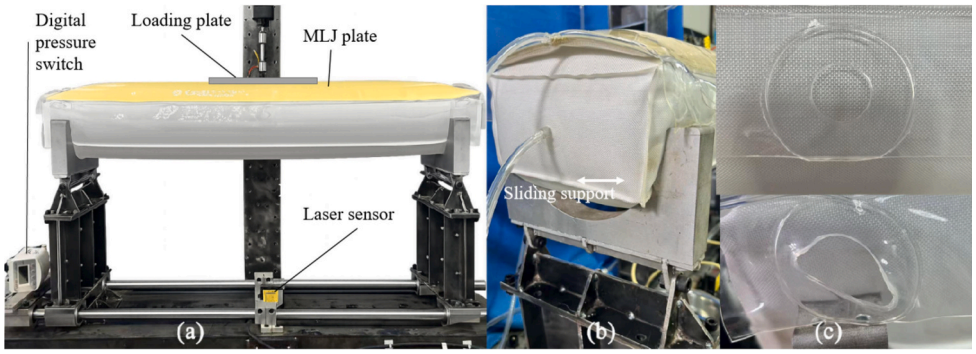


Fig. 9. Experimental setup: (a) overall testing system; (b) end views of the airbeam on specially designed semi-cylindrical supports; and (c) undeformed and deformed holes on TPU cover for cable anchorage.

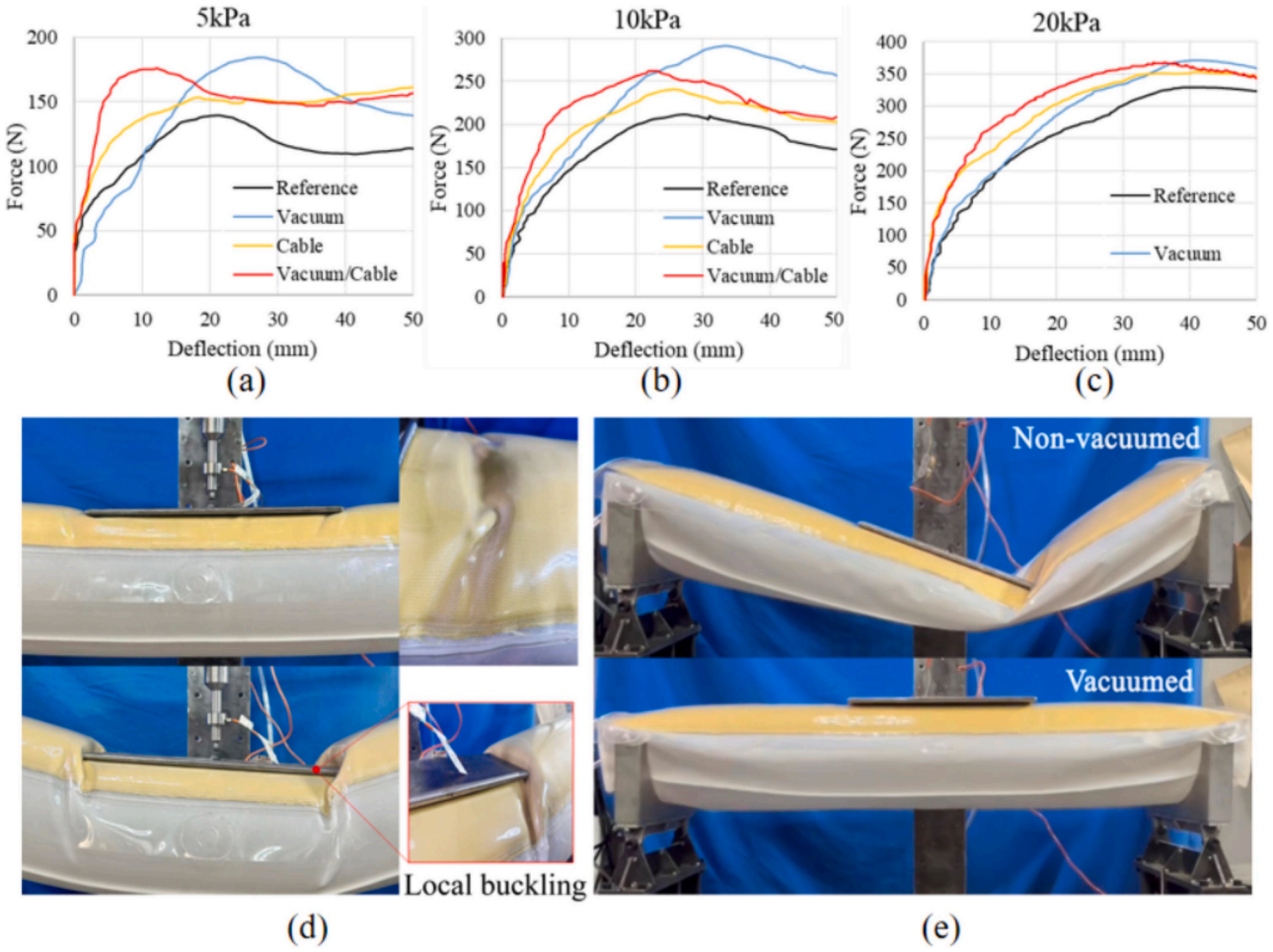


Fig. 10. Force–deflection curves under different conditions at (a) 5 kPa, (b) 10 kPa, and (c) 20 kPa: reference (no vacuum, no cable), vacuum only, cable only, and combined vacuum & cable cases; (d) local buckling development during loading; (e) deformation under air-release conditions: Non-vacuumed vs. Vacuumed.

vacuum activation and aramid fibre ropes: reference, cable only, vacuum only, and combined vacuum/cable. The internal pressure of the lower airbeam was set to 5, 10, and 20 kPa, with an accuracy of ±1 kPa (limited by the existing commercial pressure sensors). The results of the three test groups are presented in Fig. 10(a)-(c). A pneumatic loading device was used to obtain the force–displacement responses. During the initial loading stage, fluctuations were observed in the curves due to the limited precision of pneumatic control in regulating force and displacement simultaneously. However, such control accuracy is not critical for the operation of the MLJ reinforcement system, because stiffness enhancement is primarily achieved by vacuum activation of the MLJ component.

Table 3 summarises the stiffness and strength under the four configurations at 5, 10, and 20 kPa, where stiffness is calculated as the chord stiffness at 3 mm deflection. As shown in Fig. 10(a)–(c), both the aramid cables and the MLJ reinforcement increased the stiffness and ultimate load-bearing capacity of the inflatable structure. In the early loading stage, the cable reinforcement showed higher chord stiffness than the reference case, indicating that the ropes contributed to geometric restraint and early-stage force transfer. The ropes can also function as

Table 3
Stiffness and force results under different conditions at 5, 10, and 20 kPa: reference (no vacuum, no cable), vacuum only, cable only, and combined vacuum & cable cases.

Air pressure (kPa)	Results Cases	Chord stiffness (N/mm)	Difference (%)	Peak load (N)	Difference (%)
5	Reference	25.2	–	140	–
	Vacuum	14.3	–	184	32
	Cable	31.9	27	153	10
	Vacuum/ Cable	38.1	51	176	26
10	Reference	26.0	–	211	–
	Vacuum	32.1	23.5	291	38
	Cable	33.5	28.8	241	14
	Vacuum/ Cable	41.4	59.2	262	24
20	Reference	31.6	–	330	–
	Vacuum	33.6	6	371	12
	Cable	52.9	67	353	7
	Vacuum/ Cable	50.8	61	369	12

simple connection elements for assembling multiple units in parallel. However, their contribution to peak load was limited compared with the vacuum-activated MLJ plate. At all three pressure levels, the vacuum-only configuration achieved the highest ultimate load, while the cable-only case showed smaller improvements. Overall, the peak load increased by up to 38% compared with the reference case. The influence of air pressure on vacuumed and non-vacuumed configurations is further analysed in Fig. 13.

The limited contribution of the aramid fibre ropes was mainly caused by local deformation at the anchorage points. As deformation increased, the TPU membrane around the cable anchorage holes experienced severe local deformation, as shown in Fig. 9(c), which released the prestress in the ropes and weakened their restraint effect. Therefore, in the current prototype, the ropes are regarded as auxiliary tensile and connection elements rather than the primary reinforcement mechanism. In the subsequent parametric tests, the ropes were removed to isolate the effects of airbeam pressure and vacuum-activated MLJ reinforcement. With further optimisation of the rope anchorage and prestress control, the aramid fibre ropes may provide more stable tensile restraint, and the proposed system could be further developed into an MLJ-reinforced Tensairity structure [26].

During loading, the structure initially showed negligible deformation and behaved in a linear-elastic manner. Once local "buckling" occurred in the upper MLJ plate, global yielding of the structure followed. With further deformation, the structure entered a plateau stage, where deformation increased while the load increased only slightly, indicating energy dissipation. Upon unloading, the lower airbeam provided elastic support, allowing the structure to recover close to its initial position. For the vacuumed MLJ component, releasing the vacuum allowed reshaping, and the structure could be restored close to its original configuration. Fig. 10(d) illustrates the development of local buckling during loading, which typically initiated near the edges of the loading plate due to stress concentration. Fig. 10(e) shows structural response during gradual depressurization of the lower airbeam. Without MLJ vacuuming, the upper plate progressively lost stability and collapsed under the applied load as internal pressure decreased. In contrast, when vacuum was applied to the MLJ component, the structure experienced global settlement but remained straight and stable, demonstrating that the MLJ reinforcement effectively prevents collapse following air pressure loss.

3.2.3. *Quasi-static cyclic hysteresis test*

To quantitatively assess the energy dissipation capacity, hysteresis tests were performed at lower airbeam pressures of 5, 10, and 20 kPa, under both vacuumed and non-vacuumed conditions. Six displacement amplitudes D (10 mm, 20 mm, 30 mm, 60 mm, 90 mm, and 120 mm) were applied to enable a systematic parametric analysis. For accurate displacement control, the loading system was upgraded from pneumatic to hydraulic actuation, which provides higher stiffness, faster feedback response, and improved loading stability.

Representative hysteresis curves are presented in Fig. 11. Because the 10 mm amplitude case remained almost entirely within the linear-elastic regime and exhibited large signal noise, it was excluded from the loop-area-based energy analysis. During hysteresis tests, the mid-span displacement measured in the lower airbeam was consistently smaller than the imposed displacement amplitudes, as part of the applied stroke was absorbed by compressive deformation of the airbeam. As a result, actuator displacements of 20 mm, 30 mm, 60 mm, 90 mm, and 120 mm correspond approximately to measured mid-span displacements of about 6 mm, 13 mm, 30 mm, 50–60 mm, and 80–90 mm, respectively, depending on the internal pressure level. Because only the displacement at the lowest point of the airbeam was measured, without accounting for the deformation between the loading point and the measurement location, the reported displacement values are conservative. Consequently, the calculated dissipated energy values are also conservative. Although the absolute energy values may not represent the exact energy dissipation of the structure, they remain suitable for evaluating the relative improvement in energy dissipation between different test conditions. The dissipated energy E_d was quantified as the enclosed area of each hysteresis loop using Teng's method [27]. A customised analysis pipeline implemented in MATLAB automatically computed the hysteresis loop area A_{loop} for each displacement amplitude via numerical integration. The dissipated energy was directly proportional to the structural damping capacity:

$$E_d = \int F(x)\mathrm{d}x \propto A_{loop} \tag{21}$$

where E_d denotes the dissipated energy, $F(x)$ represents the difference between the loading and unloading forces, and A_{loop} is the enclosed area of the hysteresis loop. The calculated results are summarized in Table 4.

The observed energy dissipation originates from the combined mechanical interaction between the MLJ layer and the inflatable airbeam. Under cyclic loading, vacuum confinement induces normal pressure between adjacent MLJ layers, generating interlayer friction during relative sliding. This frictional slip converts mechanical work into dissipated energy. Simultaneously, deformation of the pressurized airbeam contributes additional dissipation through membrane deformation and internal gas compression–expansion effects. The coupled action of frictional sliding and inflatable compliance results in stable hysteretic behaviour.

Experimental results show that the internal pressure primarily governs load-bearing capacity, while MLJ activation significantly enhances both stiffness and dissipation behaviour. In the non-vacuumed state, the maximum load at 5, 10, and 20 kPa was approximately 140, 210, and 250 N, respectively. After full evacuation of the MLJ plate, the ultimate load increased to approximately 165, 270, and 280 N, corresponding to 18%, 29%, and 12%. The differences in reinforcement efficiency among the tested pressure levels are further analysed in the following section.

Hysteresis tests further demonstrate substantial energy dissipation after vacuum activation at all pressure levels. When the initial dissipation capacity was low, vacuuming approximately doubled the enclosed hysteresis energy. At 10 kPa, hysteresis loops appeared most stable and well-developed, with dissipated energy increasing by approximately 32–44%. At 5 kPa, sharp load reduction occurred once displacement amplitudes exceeded 90 mm, producing pinched hysteresis loops and unstable deformation behaviour despite large loop areas. At 20 kPa, although higher peak loads resulted in large absolute dissipation values, the loop-area efficiency decreased at displacement amplitudes beyond

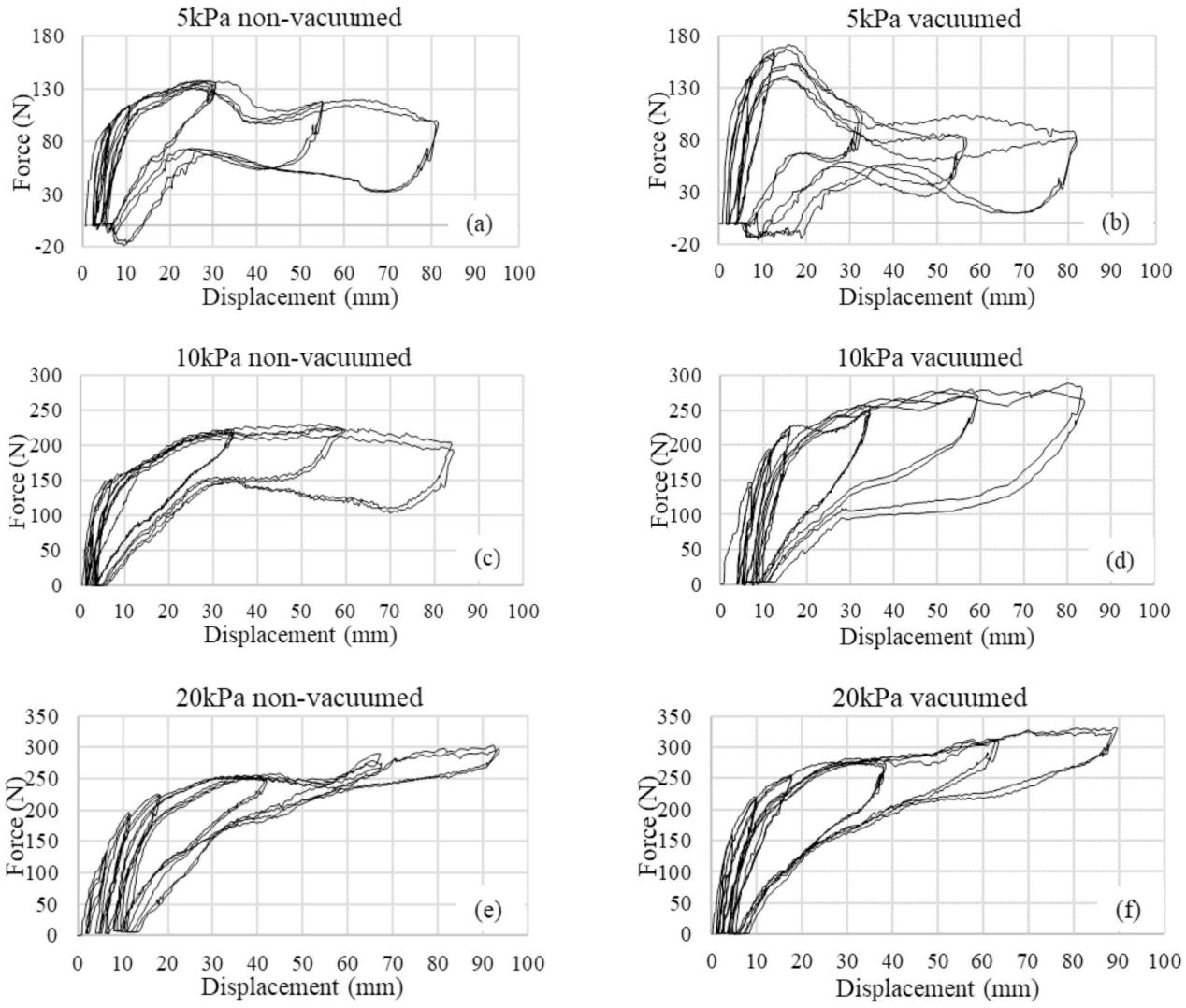


Fig. 11. Hysteresis curves of non-vacuumed & vacuumed cases: (a-b) 5 kPa, (c-d) 10 kPa, and (e-f) 20 kPa.

Table 4
Energy dissipation computed from hysteresis curves for the non-vacuumed and vacuumed cases.

Air pressure (kPa)	D (mm) E_d (mJ)	20	30	60	90	120
5	Non-vacuumed	222.43	382.8	1458.1	3193.4	5061.2
	Vacuumed	402.6	706.77	2633.2	4058.4	5964.8
	Difference (%)	81%	85%	81%	27%	18%
10	Non-vacuumed	325.12	638.37	2207.7	4111.8	6859.4
	Vacuumed	674.59	919.66	2907.6	5505.3	9385.5
	Difference (%)	107%	44%	32%	34%	37%
20	Non-vacuumed	518.46	820.2	3513.4	4712.65	4403.1
	Vacuumed	579.38	999.61	3973	4903.2	6177.5
	Difference (%)	12%	22%	13%	4%	40%

90 mm, leading to inferior performance compared with the 10 kPa case. The smaller difference observed at 20 kPa indicates that the structural response becomes increasingly dominated by the airbeam stiffness at higher internal pressure, reducing the relative contribution of MLJ reinforcement. Overall, the 10 kPa-vacuumed case provided the most balanced performance in terms of stiffness enhancement, yield stability, and energy dissipation capacity.

3.3. Experimental interpretation of the combined effect of MLJ and the airbeam

3.3.1. Airbeam

A simply supported inflatable airbeam is adopted to establish the analytical model, as illustrated in Fig. 12. Following the analytical formulation for inflated circular cylindrical beams proposed by Comer and Levy [28], the simply supported beam is treated through a half-span model under symmetric loading. The compressed region at the lower side of the cross section is assumed to wrinkle, as shown by the grey region in Fig. 12(a). In the wrinkled region, the axial membrane stress is assumed to vanish, while the remaining taut region carries axial membrane stress. The corresponding deformation mechanism is illustrated schematically in Fig. 12(b).

The angular coordinate θ_0 defines the boundary between the wrinkled and taut regions of the circular cross section. Based on the moment equilibrium and axial force equilibrium of the membrane stress re-

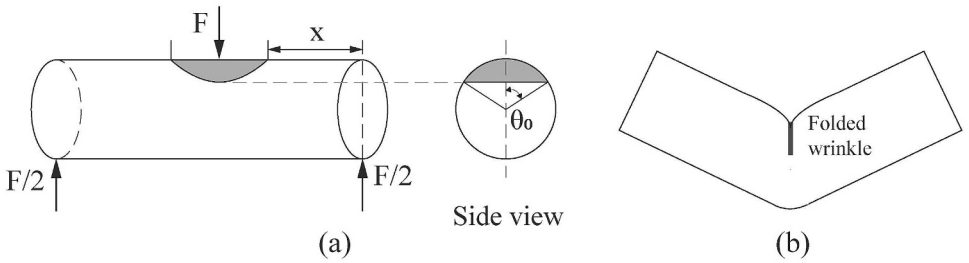


Fig. 12. Analytical model of the cylindrical airbeam: (a) loading configuration and assumed wrinkled compression region; (b) schematic deformation mechanism of the airbeam.

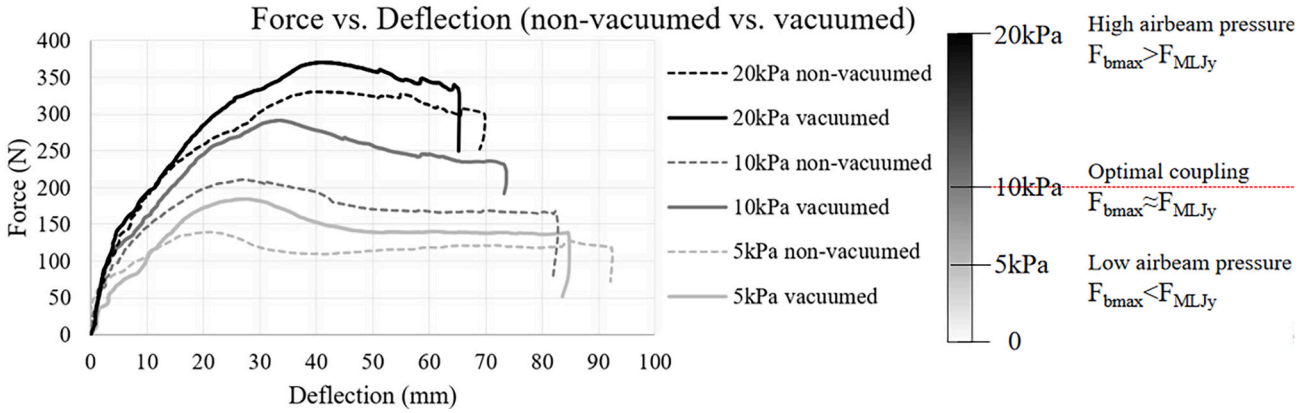


Fig. 13. Force vs. deflection curves at 5, 10, and 20 kPa: non-vacuumed vs. vacuumed. The three theoretical response regimes discussed in Section 3.3.2 are indicated on the right side according to the internal airbeam pressure.

sultants reported by Comer and Levy [28], the relationship between θ_0 and the applied force F at a section located at a distance x from the support is given by

$$\frac{2\pi - 2\theta_0 + \sin 2\theta_0}{\sin\theta_0 + (\pi - \theta_0)\cos\theta_0} = \frac{2}{\pi}\frac{Fx}{pR^3} \tag{22}$$

where p is the internal pressure and R is the radius of the circular section.

When $= \frac{L}{2}$, the section at midspan has not yet buckled, corresponding to $\theta_0 = 0$. Substituting $\theta_0 = 0$ into the above expression yields the initial buckling load

$$F = \frac{2\pi pR^3}{L} \tag{23}$$

When bending buckling fully develops, the compressed region extends over half of the circumference and $\theta_0 = \pi$. In this case, the fully developed buckling (collapse) load becomes

$$F_{max} = \frac{4\pi pR^3}{L} \tag{24}$$

which is twice the initial buckling load. This is approximately consistent with the force-deflection and hysteresis curves shown earlier, where the maximum load in the linear regime is approximately half of the peak load at collapse.

For the rectangular airbeam used in the present experiments, a direct closed-form solution is not pursued because the membrane stress distribution is affected by corner deformation, cross-sectional distortion, and local wrinkling. Instead, the circular-beam collapse solution is used as an approximate upper-bound scaling relation. To account for the different cross-sectional shape, a perimeter-based equivalent radius R is introduced. For the present tests with a rectangular section of $b \times h =$ 10 cm $\times$ 20 cm, the equivalent radius is defined as $R = \frac{b+h}{\pi}$. The perimeter-based equivalent radius is adopted because the bending resistance of an inflated thin-walled beam is governed primarily by the membrane forces distributed along its circumference, rather than by the enclosed area. The classical expression $M_c\ pR^3$ for circular inflatable beams is derived from the integration of axial and hoop membrane stresses around the perimeter. By matching the perimeter of the rectangular section to that of an equivalent circle, the resulting R more consistently preserves the effective membrane force path and thus the pressure-induced bending capacity.

In practice, the rectangular airbeam cannot fully reproduce the ideal circular-beam behaviour. At sufficiently high pressures, the membrane is strongly prestressed and the cross section is better stabilised against cross-sectional distortion and local wrinkling. At lower pressures, however, cross-sectional deformation and corner effects reduce the effective load-carrying perimeter. To account for this pressure-dependent deviation, a reduction factor $C_p \leq 1$ is introduced, representing the effectiveness of the rectangular cross section in mobilising circumferential membrane forces. Accordingly, substituting $R = \frac{b+h}{\pi}$ into the circular-beam collapse load then gives the following approximate estimate:

$$F_{max} = C_p\frac{4\pi p}{L}\left(\frac{b+h}{\pi}\right)^3 = C_p\frac{4p(b+h)^3}{\pi^2 L} \tag{25}$$

where C_p depends on internal pressure, corner deformation, cross-sectional distortion, and local wrinkling. Therefore, Eq. (25) should be interpreted as an approximate upper-bound scaling relation rather than an exact closed-form solution for a rectangular inflatable beam.

Using the same equivalent-radius approximation, the corresponding deflection can also be obtained in a non-dimensional form. The dimensionless deflection η satisfies

$$\frac{d^2\eta}{d\xi^2} = \xi\left(\frac{2}{2\pi - 2\theta_0 + \sin 2\theta_0}\right), \pi > \xi > \frac{\pi}{2}$$

$$\frac{d^2\eta}{d\xi^2} = \frac{\xi}{\pi}, \frac{\pi}{2} > \xi > 0 \tag{26}$$

where $\eta = \frac{F^2Et}{4p^3R^6}y$ and $\xi = \frac{F}{2pR^3}x$. E is the elastic modulus, t is the wall thickness of membrane, y is the physical deflection, and x is the coordinate along the beam length. Similar to Eq. (25), Eq. (26) is used here as an equivalent-radius approximation to describe the deflection trend, rather than as an exact analytical solution for the rectangular cross section.

3.3.2. Combined effect

Fig. 13 presents the force–deflection curves of the MLJ-reinforced airbeam tested at internal pressures of 5, 10, and 20 kPa, with and without vacuum applied to the upper MLJ layer. After vacuuming, both the stiffness and strength of the structure increase markedly. Specifically, the peak load increased from approximately 140 N to 184 N (32%) at 5 kPa, from 211 N to 291 N (38%) at 10 kPa, and from 330 N to 371 N (12%) at 20 kPa, respectively. These results indicate that the strengthening effect provided by the MLJ layer is pressure-dependent, where the load-bearing capacity is increasingly governed by the inflatable airbeam itself.

The measured response can be interpreted as the interaction between two competing limit mechanisms: (i) the onset of jamming failure in the upper MLJ layer, characterised by a transition from bulk-like behaviour to progressive interlayer sliding, and (ii) buckling failure of the lower airbeam [22]. For a given MLJ configuration (fixed layer number, geometry, and materials), the sequence of these two mechanisms is primarily controlled by the internal pressure of the lower airbeam. Based on the relative magnitude of $F_{MLJy} = \frac{2}{3}nbh\mu\Delta P$(Eq.(8)) and $F_{bmax} = C_p\frac{4p(b+h)^3}{\pi^2 L}$(Eq.(25)), three distinct response regimes can be theoretically identified:

(1) $F_{bmax} > F_{MLJy}$: MLJ yields first (high airbeam pressure)

At a sufficiently high airbeam pressure, the collapse capacity of the airbeam exceeds the jamming-yield load of the MLJ layer. In this regime, the response is initially governed by the bulk-like behaviour of the jammed laminate, resulting in a relatively high initial stiffness. Once the MLJ reaches its yield load, interlayer sliding initiates and the structural stiffness decreases, leading to a stable softening or yielding plateau. After MLJ yielding, the load-carrying capacity of the laminate cannot increase further and the response becomes increasingly governed by the lower airbeam. As sliding progresses, hysteretic energy dissipation increases markedly due to frictional work at the interfaces. The overall behaviour is therefore characterised by early laminate yielding followed by airbeam-dominated load transfer and enhanced energy dissipation.

(2) $F_{bmax} \approx F_{MLJy}$: near-simultaneous yielding (optimal coupling)

When the two characteristic loads are of comparable magnitude, the two mechanisms are triggered in close succession. This condition corresponds to the maximum reinforcement efficiency of the hybrid system and provides a balanced combination of stiffness retention, stable yielding, and energy dissipation. In this regime, the linear response is sustained over a larger deformation range, and the transition at the peak load is smooth rather than abrupt. The airbeam provides the primary load-bearing capacity and geometric stability, while progressive MLJ sliding stabilises the post-yield response and prevents sudden collapse. Consequently, both peak load and hysteretic energy dissipation are maximised. The difference between vacuumed and non-vacuumed cases is most pronounced in this regime, since vacuuming directly increases F_{MLJy} and shifts the system closer to the optimal balance point. This mechanism explains why the 10 kPa tests exhibit the highest overall reinforcement efficiency.

(3) $F_{bmax} < F_{MLJy}$: airbeam buckles first (low airbeam pressure)

At low internal pressure, or for slender airbeams, the airbeam may buckle before the MLJ plate reaches its yield load. In this case, geometric instability of the airbeam (buckling, wrinkling, and compression-zone development) disrupts the primary load path. If the MLJ layer is sufficiently strong, it can delay collapse and provide residual load-carrying capacity after buckling initiates. However, if the laminate strength is insufficient, it cannot fully suppress global instability and the response near the peak load becomes dominated by structural instability rather than frictional yielding. This regime is typically associated with a rapid stiffness reduction after the linear stage. In the present experiments, the 5 kPa condition does not fully enter this regime, indicating that the airbeam pressure is still high enough to avoid premature buckling.

4. Discussion

This paper proposes an MLJ-reinforced inflatable structure for rapid construction in constrained and extreme environments. Through theoretical and experimental investigations, the governing mechanisms of stiffness, strength, and energy dissipation have been identified, with particular emphasis on the role of material stiffness and friction-controlled interactions. The discussion is organised starting from material design and extending to system-level behaviour.

- **Material selection and efficiency:** A central question in MLJ system design is the selection of appropriate layer material stiffness. Analytical results show that the critical sliding load is independent of material stiffness, while the maximum pre-slip deformation is inversely proportional to stiffness. Consequently, stiffness does not directly increase load capacity but controls the deformation range available for activating interlayer friction. This leads to a fundamental design trade-off: low-stiffness materials allow larger deformation, enabling effective activation of the jamming mechanism and higher load enhancement; high-stiffness materials restrict deformation, limiting interlayer slip and reducing the effectiveness of MLJ reinforcement. Accordingly, an optimal stiffness window exists, in which sufficient deformation is achieved while maintaining structural integrity. For the present system, this corresponds approximately to the low-stiffness, high-strain regime. Within this range, the load enhancement ratio decreases with increasing material stiffness, highlighting that higher stiffness does not necessarily lead to improved reinforcement performance. The average equivalent modulus of the SC-AF layer calculated in Table 2 is approximately 1.1 GPa, which is significantly lower than the tensile modulus measured in material tests (12.2 GPa) [8]. This discrepancy arises from the specific loading conditions of the structural tests: the clamping during testing acted primarily on the TPU layers, while the embedded SC-AF fabric was not fully stretched and therefore did not effectively engage in tension. Consequently, the SC-AF layer did not realise its full tensile stiffness in the experiments, and the equivalent modulus is further reduced when the TPU cover layers are included. While the proposed approach shows clear potential, its current effectiveness is most evident for small- to medium-scale compliant structures. Future studies will focus on improving the experimental setup to better represent realistic boundary conditions and refining the structural design to activate the tensile capacity of the reinforcement material. The use of high-modulus SC-AF was motivated by its excellent toughness and folding durability, which are essential for deployable and inflatable applications. In subsequent work, this material will be further explored for mould-free, self-forming composite curved panels manufactured via vacuum-assisted processes. In addition, a scaling analysis will be conducted to quantify the size effect of MLJ reinforcement.
- **Effectiveness of MLJ reinforcement:** Rigidization technologies are commonly used in space gossamer structures to reduce collapse risk

after pressure loss. The effectiveness of MLJ reinforcement depends on the interaction between the upper MLJ plate and the lower airbeam, which is further governed by material stiffness, interlayer friction, and internal pressure. At high airbeam pressure, the benefit of MLJ reinforcement becomes limited. In this case, sliding within the MLJ laminate is activated first, while the airbeam continues to carry load. When the MLJ sliding load and airbeam buckling load are comparable, the system achieves the most efficient reinforcement condition, with balanced stiffness retention and enhanced energy dissipation. At low internal pressure, the airbeam buckles before the MLJ layer yields, and the response is dominated by global instability. These regimes highlight that MLJ effectiveness is not solely controlled by frictional capacity ($\mu\Delta P$), but also by the compatibility between material stiffness and structural deformation, which determines whether the jamming mechanism can be fully activated. In addition, the current prototype design did not include tensile cables, which could further improve load-bearing capacity. Future work will refine the prototype configuration and examine the deformation response and post-buckling behaviour of the coupled MLJ–airbeam system.

- **Experimental setup and stiffness measurement:** The pneumatic systems exhibit limited control due to air compressibility; however, precision control is not essential in this study, since the MLJ component is primarily operated at maximum vacuum to achieve stiffening. This differs from applications requiring continuous stiffness tuning, where high-precision control systems are necessary. The use of a single prototype introduced minor geometric imperfections due to repeated loading, leading to gradual stiffness degradation. At very low-pressure levels (e.g., 5 kPa), large deformation of the airbeam produced complex hysteresis behaviour, including multi-segment response and temporary negative stiffness. These observations further indicate that measured stiffness is not purely a material property, but a coupled response influenced by geometric configuration, frictional interaction, and boundary conditions. Future work will separate specimens for different tests and investigate progressive degradation mechanisms such as fatigue and cycling-induced softening.
- **Model–experiment comparison and interpretation:** The experimental results show noticeable deviations from the simplified analytical estimates. For instance, Eq. (25) predicts airbeam buckling loads of approximately 27, 55, and 110 N at internal pressures of 5, 10, and 20 kPa, respectively, while the planar MLJ yield load from Eq. (8) is about 28 N. These values are significantly lower than those observed experimentally, indicating that the simplified model does not fully capture the load-transfer mechanisms in the combined system. One contributing factor is the loading configuration. In the experiments, loads were applied through a finite steel plate (300 × 90 mm) rather than as a point load. This distributed loading reduces the peak bending moment, resulting in an estimated increase of approximately 18%. However, this effect alone cannot explain the discrepancy. The dominant contribution originates from the geometric transformation of the MLJ laminate after inflation. Measurements show that the MLJ layer forms a shallow curved configuration (rise ≈ 30 mm over a 200 mm span), corresponding to a radius-to-thickness ratio of Rc/t ≈ 17, placing it within a shallow-shell regime. In addition, the airbeam is supported on semi-cylindrical supports, introducing rotational restraint through contact and friction. Together with the distributed loading plate, this configuration creates geometric confinement between the airbeam and the MLJ laminate. The combined effects of curvature, distributed loading, and contact confinement generate compressive force paths within the MLJ layer, leading to shell-like stiffening mechanisms not captured by the simplified model. To account for this behaviour, a geometry-dependent factor α is introduced to relate the effective MLJ yield load to the planar prediction. This factor represents the relative contribution of bending and interlayer shear to the total internal force, i.e. α∼(bending + shear)/(total force). A representative range of α ≈ 0.2-0.5 is adopted. The corresponding effective MLJ yield load is approximately 56-140 N, spanning the predicted airbeam buckling load at internal pressures of 10-20 kPa. Therefore, the simplified formulation should be interpreted as a conceptual description of the governing mechanisms, rather than a precise predictive model. More advanced models incorporating shell behaviour, cross-sectional evolution, and post-buckling interaction are required for accurate prediction.
- **Application opportunities and limitations:** The concept is particularly promising in scenarios where confinement pressure exists or can be intentionally introduced, such as in geotechnical or underwater environments (e.g., soil confinement or hydrostatic pressure in submarines). The “extreme environments” discussed here primarily refer to terrestrial conditions. For extraterrestrial applications—especially on the lunar surface—external confinement may be provided by a regolith protection layer, while internal pressurization offers an additional compressive constraint. Two potential design configurations for lunar construction are illustrated in Fig. 14. In the first configuration, the MLJ system is arranged on the inner side of the membrane, where confinement pressure is generated through the combined effect of the internal pressure differential (maintained at 1 atm inside and vacuum outside), the pressure from the protective regolith layer, and the radial force component resolved from membrane tension. In the second configuration, the MLJ system is positioned on the outer side, where membrane tension balances with the internal pressure of the inflatable structure. Under this arrangement, confinement pressure is produced by one-sided compression from external lunar soil pressure. Future work will explore additional confinement-generation scenarios to further support the effective performance of MLJ reinforcement. Although the present study uses flat and shallow-curved MLJ components as laboratory-scale demonstrators, the same mechanism can be extended to dome-shaped, arch, or shell-like structures by considering the curved surface as an assembly of local MLJ segments. In such geometries, vacuum-induced normal pressure constrains interlayer sliding and increases local bending stiffness, but overly stiff layers may reduce curvature conformity and interlayer contact. Flexible and high-strain layer materials are therefore more suitable for curved MLJ systems requiring effective contact and reversible jamming behaviour. From a scaling perspective, the frictional resistance generated by the MLJ laminate is proportional to the interlayer contact area ($\propto L^2$), while structural mass scales with volume ($\propto L^3$). As a result, the relative effectiveness of friction-based reinforcement decreases with increasing structural size. To compensate, larger systems require increased layer numbers, laminate thickness, or higher material stiffness to maintain similar structural performance.

5. Conclusion

This study presents an MLJ-reinforced inflatable system and identifies a material stiffness design window for effective jamming behaviour, enabling reversible rigidization of inflatable membranes while enhancing energy dissipation for rapid construction and multifunctional use. The design window provides a quantitative basis for material selection: within this range, the load enhancement ratio decreases with increasing material stiffness, with an upper bound of n^2-1 and a lower bound approaching zero. At the system level, the integration of multilayer jamming with inflatable structures reveals a coupled mechanical behaviour between MLJ sliding and airbeam buckling. The lower airbeam pressure governs the load capacity, while the jammed laminate provides stabilisation against collapse, particularly at reduced internal pressure. The reinforcement efficiency is maximised when the buckling loads of the MLJ plate and the airbeam are comparable. Experimental results show that, for a 1 m airbeam, the 10 kPa vacuum condition provides the best balance between stiffness retention, stable yielding,

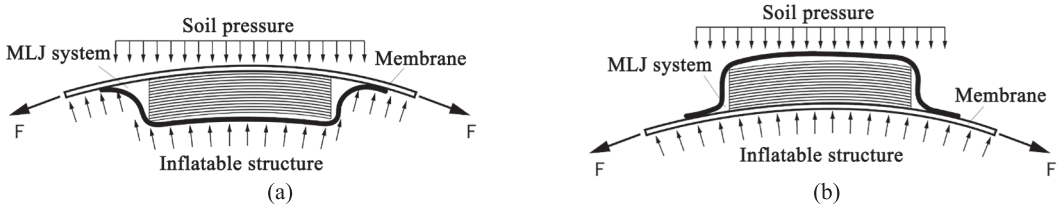


Fig. 14. Possible application scenarios for lunar construction: (a) MLJ system on the inner side; (b) MLJ system on the outer side of the membrane.

and energy dissipation. Under this condition, hysteretic energy dissipation increases by 32–44%, while the ultimate load capacity improves by up to 38%. The effectiveness of the MLJ system depends on layer number, material properties, and available confinement pressure, and becomes more pronounced at lower internal pressures. The proposed system is particularly suitable for confined or constrained environments, such as geotechnical or underwater applications, and extends the use of rigidizable inflatable structures beyond aerospace to civil engineering, robotics, and mechanical systems. Future work will focus on improved prototype designs (e.g., incorporating tensile elements), detailed investigation of post-buckling behaviour, and systematic scaling analysis to further optimise MLJ performance.

CRediT authorship contribution statement

Qinyu Wang: Writing – review & editing, Writing – original draft, Visualization, Validation, Project administration, Methodology, Investigation, Funding acquisition, Formal analysis, Data curation, Conceptualization. **Peng Feng:** Supervision, Project administration, Methodology, Funding acquisition. **Bo Wu:** Writing – review & editing, Validation, Investigation, Formal analysis. **Mingrui Teng:** Validation, Investigation, Formal analysis. **Kaspar Jansen:** Validation, Supervision, Methodology. **Charun Bao:** Writing – review & editing, Validation.

Declaration of competing interest

The authors declare that they have no known competing financial interests or personal relationships that could have appeared to influence the work reported in this paper.

Acknowledgments

This research project has been supported by National Natural Science Foundation of China (52308265) (524B2115), 17th China Postdoctoral Science Foundation Fellowship (2024T170487), Guoqiang Institute, Tsinghua University (2021GQG1001), China Postdoctoral International Exchange Program (YJ20220280), and Shuimu Tsinghua Scholar Program, and Key Technologies R&D Program of CNBM (2023SJYL04).

Appendix A

When the TPU outer membranes are considered, the total thickness becomes $nh + 2h_0$, where h_0 is the TPU thickness and E_0 is the TPU modulus. The load–deflection relationship is modified to

$$\omega_0 = \frac{FL^3}{48E_{eff}I} \tag{A1}$$

where the effective modulus of the composite section is

$$E_{eff} = E_0 + (E - E_0)\left(\frac{nh}{nh + 2h_0}\right)^3 \tag{A2}$$

and second moment of area is

$$I = \frac{1}{12}b(nh + 2h_0)^3 \tag{A3}$$

Accordingly, the interlayer shear stress at the ith interface is given by

$$\tau_{inter,i} = \frac{3F}{4b(nh + 2h_0)}\left[1 - \left(\frac{nh - 2ih}{nh + 2h_0}\right)^2\right] \tag{A4}$$

Thus, the maximum interface shear in Eq. (5) becomes

$$\tau_{inter,max} = \begin{cases} \dfrac{3F}{4b(nh + 2h_0)}, & n\ even \\ \dfrac{3F}{4b(nh + 2h_0)}\left[1 - \left(\dfrac{h}{nh + 2h_0}\right)^2\right], & n\ odd \end{cases} \tag{A5}$$

Combining Eqs. (6)–(8), (A1)-(A5), the maximum deflection and load in the presence of TPU outer layers are

$$\omega_{max} = \frac{\mu \Delta P L^3}{3E_{eff}(nh + 2h_0)^2} \tag{A6}$$

$$F_{max} = \frac{4}{3} b(nh + 2h_0)\mu \Delta P \tag{A7}$$

For two fixed supports, the load–deflection relation becomes

$$\omega_0 = \frac{FL^3}{192E_{eff}I} \tag{A8}$$

Since the shear-force distribution remains identical to that of the simply supported case, the interlayer shear expressions remain unchanged. The sliding limits at small strains are therefore

$$\omega_{max} = \frac{\mu \Delta P L^3}{12E_{eff}(nh + 2h_0)^2} \tag{A9}$$

$$F_{max} = \frac{4}{3} b(nh + 2h_0)\mu \Delta P \tag{A10}$$

Data availability

Data will be made available on request.

References

[1] I.K. Kuder, A.F. Arrieta, W.E. Raither, P. Ermanni, Variable stiffness material and structural concepts for morphing applications, Prog. Aerosp. Sci. 63 (2013) 33–55.

[2] R. D. Kornbluh, H. Prahlad, R. Pelrine, S. Stanford, M. A. Rosenthal and P. A. von Guggenberg, "Rubber to rigid, clamped to undamped: toward composite materials with wide-range controllable stiffness and damping," in *Smart Structures and Materials 2004: Industrial and Commercial Applications of Smart Structures Technologies*, vol. 5388, International Society for Optics and Photonics, 2004, July, pp. 372-386.

[3] Q. Wang, G. Senatore, K. Jansen, A. Habraken, P. Teuffel, Design and characterization of variable stiffness structural joints, Mater. Des. 187 (2020) 108353.

[4] B. Defoort, V. Peypoudat, M.C. Bernasconi, K. Chuda, X. Coqueret, Recent advances in the rigidization of gossamer structures, Textile Compos. Inflatable Struct. (2005) 259–283.

[5] M. Schenk, A.D. Viquerat, K.A. Seffen, S.D. Guest, Review of inflatable booms for deployable space structures: packing and rigidization, J. Spacecr. Rocket. 51 (3) (2014) 762–778.

[6] J. Lin, C. Knoll and C. Willey, "Shape memory rigidizable inflatable (RI) structures for large space systems applications," in *47th AIAA/ASME/ASCE/AHS/ASC Structures, Structural Dynamics, and Materials Conference 14th AIAA/ASME/AHS Adaptive Structures Conference 7th*, 2006.

[7] Q. Wang, P. Feng, K. Jansen, C. Bao, A novel rigidizable inflatable lunar habitation system: design concept and material characterization, Mater. Des. 246 (2024) 113289.

[8] Q. Wang, P. Feng, B. Wu, J. Zhao, J. Tang, K. Jansen, Rigidization capacity and folding behavior of variable stiffness composite skin for inflatable lunar habitats, Compos. A Appl. Sci. Manuf. (2025) 109169.

[9] Y.S. Narang, B. Aktaş, S. Ornellas, J.J. Vlassak, R.D. Howe, Lightweight highly tunable jamming-based composites, Soft Rob. 7 (6) (2020) 724–735.

[10] J. Ou, L. Yao, D. Tauber, J. Steimle, R. Niiyama, H. Ishii, jamSheets: thin interfaces with tunable stiffness enabled by layer jamming. in Proceedings of the 8th international conference on tangible, embedded and embodied interaction, 2014.

[11] Y.S. Narang, A. Degirmenci, J.J. Vlassak, R.D. Howe, Transforming the dynamic response of robotic structures and systems through laminar jamming, IEEE Rob. Autom. Lett. 3 (2) (2017) 688–695.

[12] F. Caruso, G. Mantriota, V. Moramarco, G. Reina, Layer jamming: modeling and experimental validation, Int. J. Mech. Sci. 251 (2023) 108325.

[13] F. Caruso, G. Mantriota, L. Afferrante, G. Reina, A theoretical model for multi-layer jamming systems, Mech. Mach. Theory 172 (2022) 104788.

[14] S. G. Fitzgerald, G. W. Delaney and D. Howard, "A review of jamming actuation in soft robotics," *Actuators,* vol. 9, no. 4, p. 104, 2020, October.

[15] C. Mikol and H. J. Su, "An actively controlled variable stiffness structure via layer jamming and pneumatic actuation," in *2019 International Conference on Robotics and Automation (ICRA)*, 2019, May.

[16] M. Ibrahimi, L. Paternò, L. Ricotti, A. Menciassi, A layer jamming actuator for tunable stiffness and shape-changing devices, Soft Rob. 8 (1) (2021) 85–96.

[17] W.H. Choi, S. Kim, D. Lee, D. Shin, Soft, multi-DoF, variable stiffness mechanism using layer jamming for wearable robots, IEEE Rob. Autom. Lett. 4 (3) (2019) 2539–2546.

[18] D.S. Shah, E.J. Yang, M.C. Yuen, E.C. Huang, R. Kramer-Bottiglio, Jamming skins that control system rigidity from the surface, Adv. Funct. Mater. 31 (1) (2021) 2006915.

[19] W.P. Weston-Dawkes, M.R.A. Majit, J. Sandoval, E.L.S. Ochoa, S. Horgan, M. T. Tolley, Design of layer jamming liver retractor for surgical access, deployment, and removal, IEEE Trans. Med. Rob. Bionics 6 (1) (2024) 317–327.

[20] H. Qi, M. Yang, X. Zhang, Y. Zhang, B. Wu, J. Liu, Review on the structural design and materials of covers for inflatable lunar habitat (in Chinese), Spacecraft Environ. Eng. 38 (6) (2021) 715–722.

[21] Q. Wang, P. Feng, K. Jansen, Designs of self-rigidizable inflatable habitats for construction in extreme environments. in Proceedings of IASS Annual Symposia, 2024.

[22] W. P. Weston-Dawkes and M. T. Tolley, "Jamming-reinforced inflatable beams for mobile robotics," in *International Design Engineering Technical Conferences and Computers and Information in Engineering Conference*, American Society of Mechanical Engineers, 2022, August.

[23] B. Aktaş, Y.S. Narang, N. Vasios, K. Bertoldi, R.D. Howe, A modeling framework for jamming structures, Adv. Funct. Mater. 31 (16) (2021) 2007554.

[24] R. Acevedo, L. Santos, R.D. Pedersen, N. Goyal, N.M. Bruck, S.K. Gupta, H. A. Bruck, Characterization and modeling of layer jamming for designing engineering materials with programmable elastic-plastic behavior, Exp. Mech. 60 (9) (2020) 1187–1203.

[25] Q. Wang, P. Feng, L. Dong, K. Jansen, A novel multi-layer jamming (MLJ)-reinforced Tensairity beam for rapid construction in extreme environments. Proceedings of IABSE Congress Ghent 2025 —— The Essence of Structural Engineering for Society, 2025.

[26] R. H. Luchsinger, A. Pedretti, P. Steingruber and M. Pedretti, "The new structural concept Tensairity: Basic principles," *Progress in structural engineering, mechanics and computation,* pp. 323-328, 2004.

[27] M. Teng, P. Feng, H. Lin, Z. Qu, Seismic performance analysis based on hysteresis curve data: Index definition, algorithm optimization, and program implementation (in Chinese), Eng. Mech. 42 (7) (2023) 89–101.

[28] R.L. Comer, S. Levy, Deflections of an inflated circular cylindrical cantilever beam, AIAA J. 1 (7) (1963) 1652–1655.